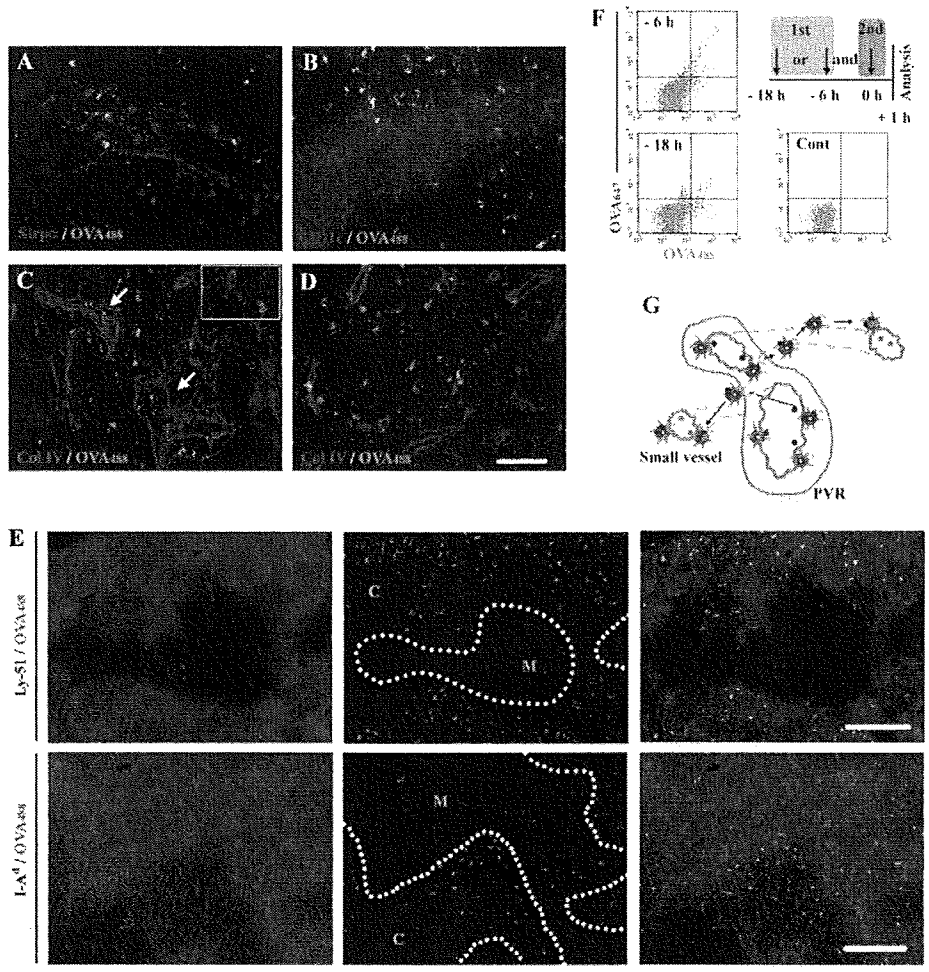

FIGURE 5. Localization of i.v. injected Ag in thymus. *A–C*, Thymic tissues were obtained 0.5 h after injection of OVA_{488} and were stained to obtain a double-color fluorescent image with the combination of OVA_{488} (green) and (*A*) Sirpα (red), (*B*) CD11c (red), or (*C*) Col IV (red). Arrows in *C* indicate the cells with captured OVA_{488} inside the PVRs. The image showing the cells capturing OVA_{488} in close proximity to small vessels is an *inset* in *C*. *D*, A double-color fluorescent image for OVA_{488} (green) and Col IV (red) at 6 h after OVA injection. Scale bars, 100 μm. *E*, A double-color fluorescent image with the combination of OVA_{488} (green) and Ly51 (red) or I-A^d (red) at 18 h after injection is shown in the *upper* and *lower panels*, respectively. The merged images are shown in the *right panels*. Dashed lines indicate the boundary between cortex (C) and medulla (M). Scale bars, 200 μm. *F*, OVA_{647} and OVA_{488} were i.v. injected consequently with an interval of either 6 or 18 h, illustrated in *upper right panel* in *F*. Uptake of OVA protein by $CD11c^{high}$ DC population isolated after double injection with an interval of either 6 or 18 h is shown in the *left upper* and *lower panels*, respectively. Autofluorescence for each parameter in the $CD11c^{high}$ DC population without injection is shown as a control. Representative results from three independent experiments are shown here. *G*, Presumed intrathymic trafficking modes of Sirpα^- DCs, combined with the Ag uptake. Blue and green particles indicate OVA_{647} and OVA_{488}, respectively.

result in enhanced accumulation of autoreactive T cells against serum self-Ags.

Discussion

Mouse thymus $CD11c^+$ cDCs can be classified into two populations, a major $CD8\alpha^+$ and a minor $CD8\alpha^-$ one (31). $CD8\alpha^-$ cDCs can pick up $CD8\alpha\beta$ heterodimer from thymocytes and retain them on the cell surface, thus precluding the use of $CD8\alpha$ as a reliable marker to distinguish these two populations. Wu and Shortman (8) observed that $CD8\alpha^-$ but not $CD8\alpha^+$ cDCs simultaneously express the Sirpα molecule and proposed the use of Sirpα as a marker of this minor cDC population. Concomitantly, it was proposed that the interaction between thymocytes and DCs in thymic cortex can also have profound effects on positive selection (32). Likewise, McCaughtry et al. (33) observed that clonal deletion of autoreactive thymocytes requires the stimuli from rare $CD11c^+$ cortical DCs. Given the unique localization of Sirpα^+ DCs confined to the cortex, these observations suggest the potential involvement of Sirpα^+ DCs in central tolerance, but their small number hinders the isolation for a detailed analysis of Sirpα^+ DC function.

A partial but selective reduction in intrathymic Sirpα^+ cDCs in $CCR2^{-/-}$ mice prompted us to investigate the thymic selection process in WT and $CCR2^{-/-}$ mice to elucidate the role of intrathymic Sirpα^+ cDCs in the process. When DO11.10 TCR-transgenic mice were administered immunogenic $OVA_{323-339}$ peptide i.v., *CCR2* gene ablation partially attenuated the clonal negative deletion by apoptosis of the $DO11.10^+$ DP thymocyte population. Intraperitoneal injection of anti-CD3 Ab deleted thymocytes to similar extents in WT and $CCR2^{-/-}$ mice, excluding the possibility that CCR2 deficiency impaired the apoptotic response of thymocytes. Negative selection can be exerted by various types of APCs including Sirpα^- cDCs, B cells, macrophages, cortical thymic epithelial cells, and mTEC in addition to Sirpα^+ cDCs. We

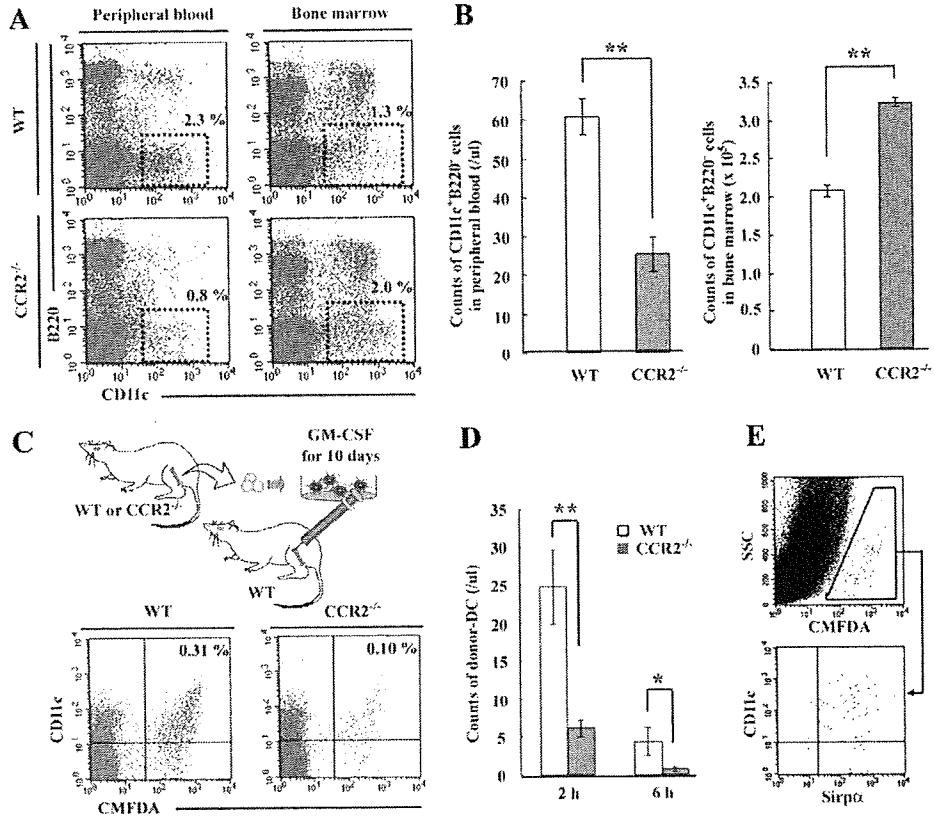

FIGURE 6. Mobilization of Sirpα$^+$ DCs from bone marrow. *A* and *B*, PBMCs and bone marrow cells isolated from femur bone marrow were stained with anti-CD11c and anti-B220 mAbs. Proportion (*A*) and the numbers (*B*) of CD11c$^+$ B220$^-$ cells gated with the dot squares were determined on peripheral blood and bone marrow in CCR2$^{-/-}$ and WT mice. Percentage of gated cells is shown in each panel of *A*. Mean ± SD were calculated from three independent experiments and are shown here. *C*, The image of experimental procedure of "trafficking of bone marrow-derived DCs" was illustrated and is shown in the *upper panel*. PBMCs were isolated from the recipients 2 h after injection and stained with anti-CD11c mAb. Egress of CCR2$^{-/-}$ bone marrow-derived DCs into peripheral blood was compared with WT DCs. Percentage of donor DCs in CMFDA$^+$CD11c$^+$ region is shown in each panel. *D*, The numbers of donor-derived DCs in peripheral blood were determined 2 and 6 h after injection. Mean ± SD calculated from five independent experiments are shown here. *, $p < 0.05$ and **, $p < 0.01$. *E*, One × 10^7 WT bone marrow cell-derived DCs were injected into both the right and left tibial cavity. Six hours after injection, expression of Sirpα and CD11c on intrathymic migrated CMFDA$^+$ donor cells was analyzed by FCM. Representative results from four independent experiments are shown here.

failed to detect any apparent differences in other APC populations than Sirpα$^+$ cDCs between WT and CCR2$^{-/-}$ mice. Thus, it is unlikely that reduced negative selection in CCR2$^{-/-}$ mice can be ascribed to the changes in these cell populations. Furthermore, accumulating evidence implicates intrathymic CD4$^+$CD25$^+$ regulatory T cells as an essential cell component in central tolerance.

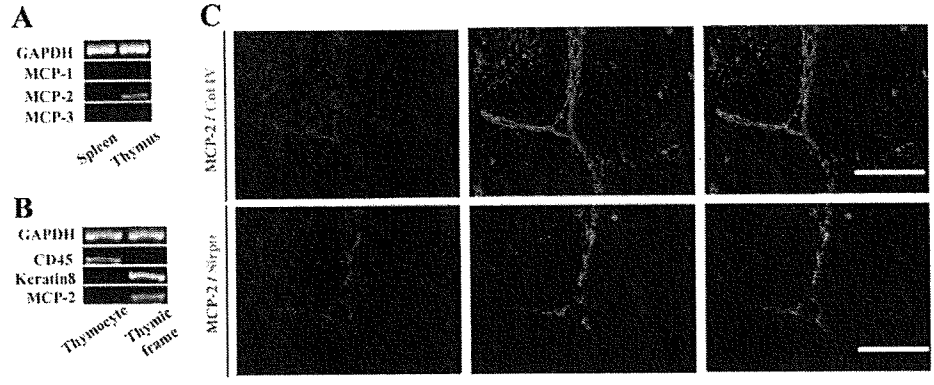

FIGURE 7. Expression of CCR2 ligands in thymus under physiological condition. *A*, Total RNAs were extracted from thymus and spleen of WT mice. Expression of CCR2 ligands, MCP-1, MCP-2, and MCP-3, was determined by RT-PCR. GAPDH served as an internal positive control. *B*, Thymic tissues were mechanically disrupted and fractionated into thymocyte and thymic stromal components. MCP-2 transcripts were determined on these two fractions by RT-PCR. CD45 and keratin 8 served as positive control for the thymocyte and thymic stromal fraction, respectively. *C*, Double-color fluorescent immunostaining for MCP-2 (red) and Col IV (green) or MCP-2 (red) and Sirpα (green) in the thymic tissue sections are shown in the *upper* and *lower panels*, respectively. The merged images are shown in the *right panels*. Representative results from three independent animals are shown here. Scale bars, 100 μm.

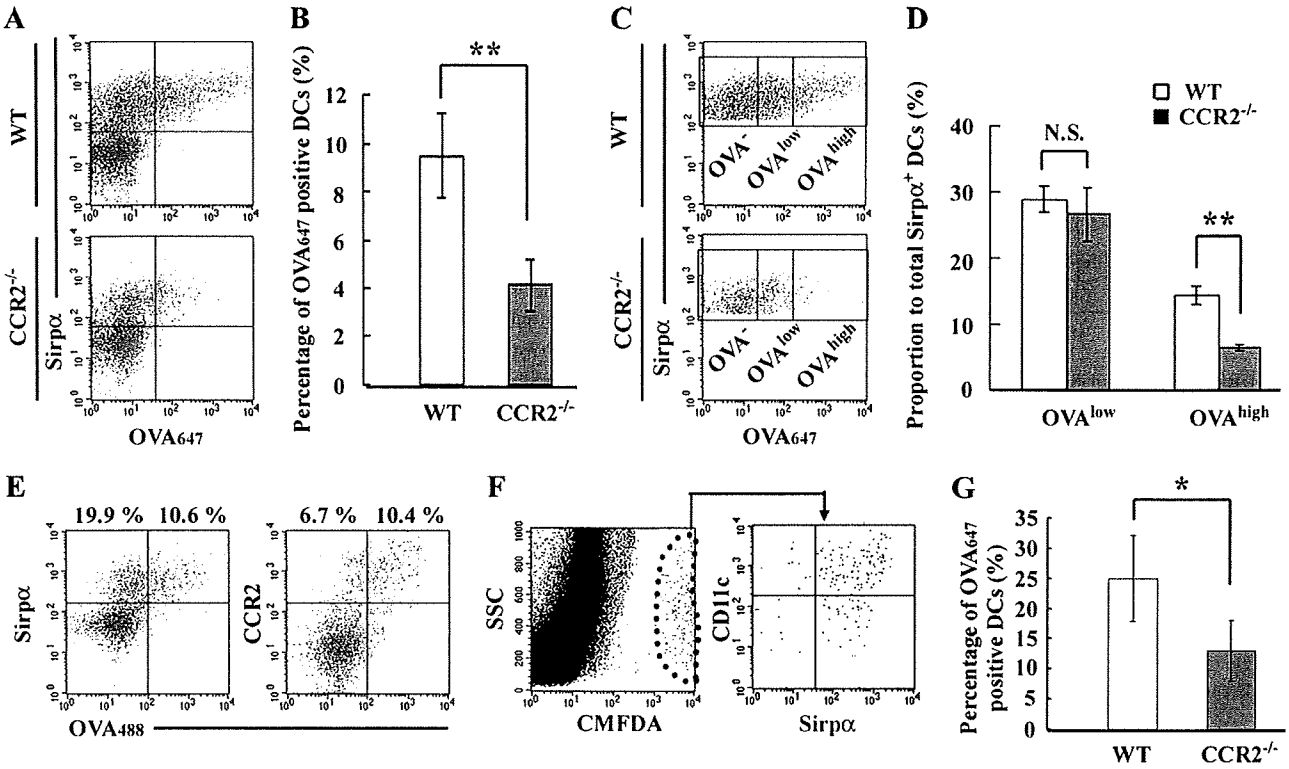

FIGURE 8. Effects of CCR2 deficiency on Ag uptake by thymic Sirpα^+ DCs. *A*, The uptake of OVA_{647} in the CCR2$^{-/-}$ CD11c^{high} DC population at 4 h after i.v. injection was compared with WT-derived cells. *B*, Percentage of DCs capturing OVA_{647} in the CD11c^{high} DC population. Mean ± SD were calculated from five independent experiments and are shown here. **, $p < 0.01$ *C*, Sirpα^+ DCs derived from WT and CCR2$^{-/-}$ thymus were separated into three groups according to the efficiency of OVA_{647} uptake, OVA$^-$; DCs without capturing OVA_{647}, OVA^{low}; DCs capturing OVA_{647} with a low efficiency, and OVA^{high}; and DCs capturing OVA_{647} with a high efficiency. *D*, Percentage of OVA^{low} and OVA^{high} in WT and the CCR2$^{-/-}$ Sirpα^- DC population. Mean ± SD were calculated from five independent experiments and are shown here. **, $p < 0.01$; N.S., no significant difference. *E*, OVA_{488} was i.v. injected into WT mice. One hour after injection, low-density cells were stained with anti-CD11c and anti-Sirpα or anti-CCR2 mAbs. The uptake of OVA_{488} and expression of Sirpα or CCR2 in the CD11c^{high} DC population are shown. Percentage of Sirpα^+OVA$_{488}^+$ and OVA$_{488}^-$, or CCR2$^+$OVA$_{488}^-$ and OVA$_{488}^-$ regions are shown in the *left* or *right panel*. Representative results from three independent experiments are shown here. *F*, Migration of Sirpα^+ DCs into the thymus at 2 days after i.v. injection of CMFDA-labeled WT bone marrow cells into CCR2$^{-/-}$ mice. Expression of CD11c and Sirpα on CMFDA$^+$ donor-derived cells is shown in the *right panel*. Representative results from three independent experiments are shown here. *G*, OVA_{647} was i.v. injected into CCR2$^{-/-}$ mice at 2 days after injection of bone marrow cells. Percentage of WT and CCR2$^{-/-}$ donor-derived DCs capturing OVA_{647} in the CMFDA$^+$CD11c^{high} region are shown. Mean ± SD were calculated from four independent experiments and are shown here. *, $p < 0.05$.

Indeed, Proietto et al. (14) recently reported the capability of Sirpα^+ cDCs to induce the differentiation of regulatory T cells in vitro. However, OVA peptide injection induced the differentiation of regulatory T cells to similar extents in both DO11.10 and DO11.10/CCR2$^{-/-}$ thymus. Thus, it is probable that CCR2 deficiency reduced modestly intrathymic Sirpα^+ DCs without affecting regulatory cell induction and partially attenuated negative selection in vivo.

It remains elusive on the trafficking modes of Sirpα^+ DCs. In CCR2$^{-/-}$ mice, Sirpα^+ DCs were decreased moderately in peripheral blood and thymus, but were increased in bone marrow. Considering that CCR2 signaling can regulate the mobilization of monocytes from bone marrow to peripheral blood (34, 35), these observations raised the possibility of a defect in the trafficking of Sirpα^+ DCs from bone marrow in CCR2$^{-/-}$ mice. Indeed, WT mouse-derived Sirpα^+ DCs, injected into bone marrow, appeared first in peripheral blood and then the thymus. On the contrary, CCR2$^{-/-}$ mouse-derived Sirpα^+ DCs exhibited impairment in the egress from bone marrow to peripheral blood. These observations suggest that bone marrow-derived Sirpα^+ DCs migrated to peripheral blood in response to CCR2-mediated signals and subsequently traffic to the thymus.

In the thymus, Sirpα^+ DCs were characteristically localized in close proximity to small blood vessels and inside the PVRs, sites which are compartmentalized by a vascular basement membrane and a border membrane separating them from the thymic parenchyma (36). It is of note that Sirpα^+ cells in the PVRs were markedly decreased in CCR2$^{-/-}$ mice to a greater extent than the decrease in total Sirpα^+ cell number. Thus, intrathymic CCR2 signaling can regulate their unique localization. This notion was supported by the observation that MCP-2, a potential ligand for CCR2, was constitutively detected in the PVRs, where Sirpα^+ DCs were present.

PVRs can provide a pathway for hematopoietic progenitor cells and mature T cells to traverse from the bloodstream to the thymic parenchyma (36) and are presumed to constitute the blood-thymus barrier, which can protect the thymic parenchyma from bloodstream-derived macromolecules (28). Thus, the unique localization of Sirpα^+ cDCs in the thymus suggested their potential interactions with bloodstream-derived Ag. This assumption was strengthened by our present observation that intrathymic Sirpα^+ cDCs rapidly and specifically captured OVA protein and serum IgG following i.v. injection. Moreover, injected Ags were initially detected inside PVRs or in nearby small vessels and were subsequently in the cortical parenchyme, and the injected Ag-derived

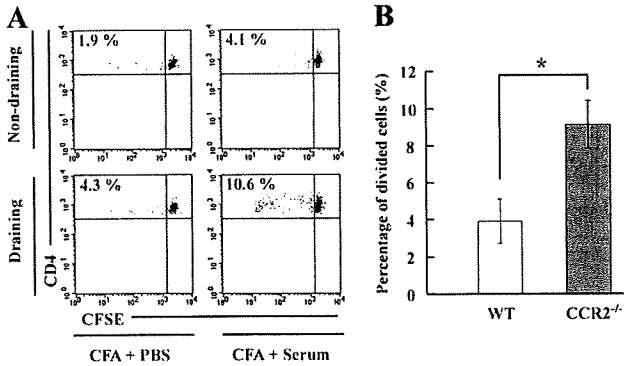

FIGURE 9. Accumulation of autoreactive T cells against serum Ags in the spleen. Spleen mononuclear cells were isolated from WT or CCR2$^{-/-}$ mice and i.v. injected into WT mice after labeling with CFSE. *A*, Recipients of CCR2$^{-/-}$ mouse-derived splenocytes were immunized with total mouse serum or PBS emulsified in CFA at 1 day after injection. Four days after, draining and nondraining lymph nodes were harvested and division of CFSE^{+} donor-derived CD4^{-} T cells was analyzed by FCM. Representative results from three independent experiments are shown here. *B*, Percentage of divided CD4^{+} T cells was determined in the draining lymph nodes of the recipients of either WT-derived or CCR2$^{-/-}$ donor-derived splenocytes when the recipients were immunized with mouse serum emulsified in CFA. Mean ± SD were calculated from three independent experiments and are shown here. *, $p < 0.01$.

signals were consistently colocalized with CD11c and Sirpα. Thus, after CD11c^{+}Sirpα^{+} cDCs, located around the PVRs, capture the Ags, they presumably move to cortical parenchyme to educate T cells. Indeed, CCR2$^{-/-}$ thymus-derived Sirpα^{+} DCs exhibited a reduced capacity to uptake OVA. The lack of CCR2 can hinder the proper intrathymic localization of Sirpα^{+} DCs and their distinctive function, Ag uptake from bloodstream, thereby reducing Ag presentation in the cortical parenchyma and subsequent negative selection against a blood-borne Ag. This hypothesis is supported by our observation in that CD4^{+} T cells reactive to certain serum self-Ags accumulated in the periphery of the recipients of CCR2$^{-/-}$ mouse-derived splenocytes to a greater extent than the recipients of WT mouse-derived splenocytes.

DCs can uptake free soluble Ags, in three distinct manners, by clathrin-mediated endocytosis, nonclathrin/caveolae endocytosis, and macropinocytosis (25). Thymic Sirpα^{+} cDCs could endocytose OVA Ags more efficiently than thymic Sirpα^{-} cDCs when they were cultured in vitro with OVA Ags. Furthermore, NH_4Cl, an inhibitor of clathrin-mediated endocytosis (26), markedly inhibited OVA endocytosis by Sirpα^{+} cDCs, but not by Sirpα^{-} cDCs. On the contrary, OVA protein endocytosis by Sirpα^{-} DCs was partially inhibited by mannan, whereas mannan had few effects on OVA protein endocytosis by Sirpα^{+} DCs. These observations suggest that thymic Sirpα^{+} cDCs characteristically can efficiently endocytose Ags in a manner distinct from thymic Sirpα^{-} cDCs.

Balazs et al. (29) reported that bloodstream DCs could efficiently capture and transport particulate bacteria into the spleen when particulate bacteria were i.v. injected. We also observed that CD11c^{+} DCs rapidly disappeared from peripheral blood after uptake of i.v. injected OVA protein. Given the capacity of CD11c^{+} DCs to move rapidly from blood to thymus, blood CD11c^{+} DCs may migrate into thymus after capturing the i.v. injected Ag. However, Ag-capturing DCs appeared very rapidly in the thymus, reaching maximal levels before disappearance of Ag-capturing circulating DCs from the peripheral blood. Furthermore, when OVA protein was injected i.v. into mice that contained bloodstream DCs labeled with fluorescent-conjugated latex beads, latex-labeled DCs did not appear in the thymus (our unpublished data). Thus, it is remotely possible that bloodstream DCs captured OVA protein and subsequently migrated into thymus.

In this study, we identified the unique intrathymic localization and functions of thymic Sirpα^{+} DCs that are involved in negative selection, particularly against blood-borne Ags. Serum protein can also induce negative selection in thymus (27, 37) but the molecular and cellular mechanisms remain to be elucidated. Because Sirpα^{+} cDCs can uptake serum protein such as IgG, these cells may induce central tolerance to blood-borne-derived Ags, in addition to Ags presented by the well-characterized intrathymic AIRE-mediated pathway.

We have shown that CCR2-mediated signals can regulate various biological aspects of Sirpα^{+} DCs such as their appropriate intrathymic localization and Ag uptake capacity. It is widely held that CCR2 might be a potential therapeutic target for several autoimmune disorders. However, because CCR2-mediated signals may contribute to thymic negative selection against blood-borne Ags, CCR2 blockade may aggravate autoimmune disorders similar to the observation on the murine collagen-induced arthritis model (38). Moreover, Lauritzsen et al (39) reported that proteins secreted from tumor cells into peripheral blood were transported into the thymus to eventually cause clonal deletion of tumor Ag-specific T cell repertoires. Given the potential capacity of intrathymic Sirpα^{+} DCs to capture blood-borne Ags, they may have a role in the development of tumor tolerance. Because human thymus contains DCs with similar phenotypes and intrathymic localization as Sirpα^{+} cDCs (40), a more detailed elucidation of the functions of Sirpα^{+} cDCs may provide us with useful insights to develop a better therapeutic strategy for cancer and stem cell transplantation as well as autoimmune disorders.

Acknowledgments

We express our gratitude to Drs. Joost J. Oppenheim (National Cancer Institute-Frederick, Frederick, MD) and Nobuyuki Onai (Akita University, Akita, Japan), and Yi Zhang (University of Michigan, Ann Arbor, MI) for critical review of this manuscript. We thank Drs. William Kuziel, Kouji Matsushima, and Philip Murphy for providing us with CCR2-, CCR5-, and CCR1- and CX3CR1-deficient mice, respectively.

Disclosures

The authors have no financial conflict of interest.

References

1. von Boehmer, H., I. Aifantis, F. Gounari, O. Azogui, L. Haughn, I. Apostolou, E. Jaeckel, F. Grassi, and L. Klein. 2003. Thymic selection revisited: how essential is it? *Immunol. Rev.* 191: 62–78.
2. Anderson, M. S., E. S. Venanzi, Z. Chen, S. P. Berzins, C. Benoist, and D. Mathis. 2005. The cellular mechanism of Aire control of T cell tolerance. *Immunity* 23: 227–239.
3. Anderson, M. S., E. S. Venanzi, L. Klein, Z. Chen, S. P. Berzins, S. J. Turley, H. von Boehmer, R. Bronson, A. Dierich, C. Benoist, and D. Mathis. 2002. Projection of an immunological self shadow within the thymus by the aire protein. *Science* 298: 1395–1401.
4. Liston, A., S. Lesage, J. Wilson, L. Peltonen, and C. C. Goodnow. 2003. Aire regulates negative selection of organ-specific T cells. *Nat. Immunol.* 4: 350–354.
5. Anderson, G., K. M. Partington, and E. J. Jenkinson. 1998. Differential effects of peptide diversity and stromal cell type in positive and negative selection in the thymus. *J. Immunol.* 161: 6599–6603.
6. Marrack, P., D. Lo, R. Brinster, R. Palmiter, L. Burkly, R. H. Flavell, and J. Kappler. 1988. The effect of thymus environment on T cell development and tolerance. *Cell* 53: 627–634.
7. Matzinger, P., and S. Guerder. 1989. Does T-cell tolerance require a dedicated antigen-presenting cell? *Nature* 338: 74–76.
8. Wu, L., and K. Shortman. 2005. Heterogeneity of thymic dendritic cells. *Semin. Immunol.* 17: 304–312.
9. Liu, Y. J. 2006. A unified theory of central tolerance in the thymus. *Trends Immunol.* 27: 215–221.
10. Bendriss-Vermare, N., C. Barthelemy, I. Durand, C. Bruand, C. Dezutter-Dambuyant, N. Moulian, S. Berrih-Aknin, C. Caux, G. Trinchieri, and F. Briere. 2001. Human

thymus contains IFN-α-producing CD11c$^-$, myeloid CD11c$^+$, and mature interdigitating dendritic cells. *J. Clin. Invest.* 107: 835–844.
11. Sprent, J., and S. R. Webb. 1995. Intrathymic and extrathymic clonal deletion of T cells. *Curr. Opin. Immunol.* 7: 196–205.
12. Heino, M., P. Peterson, N. Sillanpaa, S. Guerin, L. Wu, G. Anderson, H. S. Scott, S. E. Antonarakis, J. Kudoh, N. Shimizu, et al. 2000. RNA and protein expression of the murine *autoimmune regulator gene (Aire)* in normal, RelB-deficient and in NOD mouse. *Eur. J. Immunol.* 30: 1884–1893.
13. Kyewski, B., and J. Derbinski. 2004. Self-representation in the thymus: an extended view. *Nat. Rev. Immunol.* 4: 688–698.
14. Proietto, A. I., S. van Dommelen, P. Zhou, A. Rizzitelli, A. D'Amico, R. J. Steptoe, S. H. Naik, M. H. Lahoud, Y. Liu, P. Zheng, et al. 2008. Dendritic cells in the thymus contribute to T-regulatory cell induction. *Proc. Natl. Acad. Sci. USA* 105: 19869–19874.
15. Heinzel, K., C. Benz, and C. C. Bleul. 2007. A silent chemokine receptor regulates steady-state leukocyte homing in vivo. *Proc. Natl. Acad. Sci. USA* 104: 8421–8426.
16. Kim, C. H. 2005. The greater chemotactic network for lymphocyte trafficking: chemokines and beyond. *Curr. Opin. Hematol.* 12: 298–304.
17. Schutyser, E., A. Richmond, and J. Van Damme. 2005. Involvement of CC chemokine ligand 18 (CCL18) in normal and pathological processes. *J. Leukocyte Biol.* 78: 14–26.
18. Vecchi, A., L. Massimiliano, S. Ramponi, W. Luini, S. Bernasconi, R. Bonecchi, P. Allavena, M. Parmentier, A. Mantovani, and S. Sozzani. 1999. Differential responsiveness to constitutive vs. inducible chemokines of immature and mature mouse dendritic cells. *J. Leukocyte Biol.* 66: 489–494.
19. Niess, J. H., S. Brand, X. Gu, L. Landsman, S. Jung, B. A. McCormick, J. M. Vyas, M. Boes, H. L. Ploegh, J. G. Fox, et al. 2005. CX3CR1-mediated dendritic cell access to the intestinal lumen and bacterial clearance. *Science* 307: 254–258.
20. Gao, J. L., T. A. Wynn, Y. Chang, E. J. Lee, H. E. Broxmeyer, S. Cooper, H. L. Tiffany, H. Westphal, J. Kwon-Chung, and P. M. Murphy. 1997. Impaired host defense, hematopoiesis, granulomatous inflammation and type 1-type 2 cytokine balance in mice lacking CC chemokine receptor 1. *J. Exp. Med.* 185: 1959–1968.
21. Combadiere, C., S. Potteaux, J. L. Gao, B. Esposito, S. Casanova, E. J. Lee, P. Debre, A. Tedgui, P. M. Murphy, and Z. Mallat. 2003. Decreased atherosclerotic lesion formation in CX3CR1/apolipoprotein E double knockout mice. *Circulation* 107: 1009–1016.
22. Murai, M., H. Yoneyama, T. Ezaki, M. Suematsu, Y. Terashima, A. Harada, H. Hamada, H. Asakura, H. Ishikawa, and K. Matsushima. 2003. Peyer's patch is the essential site in initiating murine acute and lethal graft-versus-host reaction. *Nat. Immunol.* 4: 154–160.
23. Kuziel, W. A., S. J. Morgan, T. C. Dawson, S. Griffin, O. Smithies, K. Ley, and N. Maeda. 1997. Severe reduction in leukocyte adhesion and monocyte extravasation in mice deficient in CC chemokine receptor 2. *Proc. Natl. Acad. Sci. USA* 94: 12053–12058.
24. Brewer, J. A., O. Kanagawa, B. P. Sleckman, and L. J. Muglia. 2002. Thymocyte apoptosis induced by T cell activation is mediated by glucocorticoids in vivo. *J. Immunol.* 169: 1837–1843.
25. Mayor, S., and R. E. Pagano. 2007. Pathways of clathrin-independent endocytosis. *Nat. Rev. Mol. Cell Biol.* 8: 603–612.
26. Sandvig, K., S. Olsnes, O. W. Petersen, and B. van Deurs. 1987. Acidification of the cytosol inhibits endocytosis from coated pits. *J. Cell Biol.* 105: 679–689.
27. Zal, T., A. Volkmann, and B. Stockinger. 1994. Mechanisms of tolerance induction in major histocompatibility complex class II-restricted T cells specific for a blood-borne self-antigen. *J. Exp. Med.* 180: 2089–2099.
28. Bubanovic, I. V. 2003. Failure of blood-thymus barrier as a mechanism of tumor and trophoblast escape. *Med. Hypotheses* 60: 315–320.
29. Balazs, M., F. Martin, T. Zhou, and J. Kearney. 2002. Blood dendritic cells interact with splenic marginal zone B cells to initiate T-independent immune responses. *Immunity* 17: 341–352.
30. Murphy, P. M., M. Baggiolini, I. F. Charo, C. A. Hebert, R. Horuk, K. Matsushima, L. H. Miller, J. J. Oppenheim, and C. A. Power. 2000. International union of pharmacology: XXII. Nomenclature for chemokine receptors. *Pharmacol. Rev.* 52: 145–176.
31. Vremec, D., J. Pooley, H. Hochrein, L. Wu, and K. Shortman. 2000. CD4 and CD8 expression by dendritic cell subtypes in mouse thymus and spleen. *J. Immunol.* 164: 2978–2986.
32. Ladi, E., T. A. Schwickert, T. Chtanova, Y. Chen, P. Herzmark, X. Yin, H. Aaron, S. W. Chan, M. Lipp, B. Roysam, and E. A. Robey. 2008. Thymocyte-dendritic cell interactions near sources of CCR7 ligands in the thymic cortex. *J. Immunol.* 181: 7014–7023.
33. McCaughtry, T. M., T. A. Baldwin, M. S. Wilken, and K. A. Hogquist. 2008. Clonal deletion of thymocytes can occur in the cortex with no involvement of the medulla. *J. Exp. Med.* 205: 2575–2584.
34. Sawanobori, Y., S. Ueha, M. Kurachi, T. Shimaoka, J. E. Talmadge, J. Abe, Y. Shono, M. Kitabatake, K. Kakimi, N. Mukaida, and K. Matsushima. 2008. Chemokine-mediated rapid turnover of myeloid-derived suppressor cells in tumor-bearing mice. *Blood* 111: 5457–5466.
35. Tsou, C. L., W. Peters, Y. Si, S. Slaymaker, A. M. Aslanian, S. P. Weisberg, M. Mack, and I. F. Charo. 2007. Critical roles for CCR2 and MCP-3 in monocyte mobilization from bone marrow and recruitment to inflammatory sites. *J. Clin. Invest.* 117: 902–909.
36. Mori, K., M. Itoi, N. Tsukamoto, H. Kubo, and T. Amagai. 2007. The perivascular space as a path of hematopoietic progenitor cells and mature T cells between the blood circulation and the thymic parenchyma. *Int. Immunol.* 19: 745–753.
37. Haribhai, D., D. Engle, M. Meyer, D. Donermeyer, J. M. White, and C. B. Williams. 2003. A threshold for central T cell tolerance to an inducible serum protein. *J. Immunol.* 170: 3007–3014.
38. Quinones, M. P., S. K. Ahuja, F. Jimenez, J. Schaefer, E. Garavito, A. Rao, G. Chenaux, R. L. Reddick, W. A. Kuziel, and S. S. Ahuja. 2004. Experimental arthritis in CC chemokine receptor 2-null mice closely mimics severe human rheumatoid arthritis. *J. Clin. Invest.* 113: 856–866.
39. Lauritzsen, G. F., P. O. Hofgaard, K. Schenck, and B. Bogen. 1998. Clonal deletion of thymocytes as a tumor escape mechanism. *Int. J. Cancer* 78: 216–222.
40. Paessens, L. C., D. M. Fluitsma, and Y. van Kooyk. 2008. Haematopoietic antigen-presenting cells in the human thymic cortex: evidence for a role in selection and removal of apoptotic thymocytes. *J. Pathol.* 214: 96–103.

Virtual Puncture Line in Radiofrequency Ablation for Hepatocellular Carcinoma of the Caudate Lobe

Masashi Hirooka[1]
Yoshiyasu Kisaka
Kazuhiro Uesugi
Yohei Koizumi
Masanori Abe
Yoichi Hiasa
Morikazu Onji

OBJECTIVE. In this study, we evaluated the feasibility of using a virtual puncture line in 3D CT for the treatment of 21 hepatocellular carcinoma (HCC) nodules in the caudate lobe.

CONCLUSION. There were no severe complications in this study. Thus, the treatment of HCC nodules in the caudate lobe using a virtual puncture line is feasible.

Hepatocellular carcinoma (HCC) arising in the caudate lobe of the liver is not usual. The caudate lobe is located deep between the hepatic hilum and inferior vena cava. Percutaneous local ablation therapy is risky. Thus, treatment of HCC in the caudate lobe is limited because of the difficulty in accessing the lesion safely. It is important to select the puncture route using imaging guidance with various techniques, such as CT, CT arterial portography, or CT hepatic arteriography. In this study, we evaluated the feasibility and safety of using a virtual puncture line in 3D CT for the treatment of HCC in the caudate lobe.

Technique

Virtual Puncture Line

For synthesis of 3D images and generation of virtual ultrasound images, Virtual Place Advance software (AZE) was used. First, a 3D image was synthesized by CT (LightSpeed Ultra 16, GE Healthcare). The scanning parameters were 0.625-mm collimation × 16; pitch, 1.75; table speed, 300–400 mA; 120 kV; and 512 × 512 matrix. After imaging, a virtual sonogram of the CT image was generated. Virtual sonography was reshaping the CT image to a convex probe-like image on ultrasound. The dotted line showing the planned puncture line was shown on the virtual sonogram (Fig. 1C). This virtual puncture line was reflected on other 3D images synthesized by CT (Fig. 1D). This 3D image including the virtual image can be viewed from any angle, and the anatomic structure can be analyzed in detail.

Radiofrequency Ablation

Before treatment, 15 mg of pentazocine hydrochloride and 25 mg of hydroxyzine hydrochloride were administered intramuscularly. Local anesthesia was induced by 5 mL of 1% lidocaine injected through the skin into the peritoneum along a predetermined puncture line. We inserted a 20-cm-long, 17-gauge radiofrequency electrode equipped with a 2-cm-long exposed metallic tip (Cooltip, Valleylab). First, abdominal CT was performed and a virtual sonogram of the CT was prepared using the CT data. The most moderate image from the virtual ultrasound that was not deemed to be of important vessels or organs was determined by examining the various oblique axes. The virtual puncture line was made on the virtual sonogram. We confirmed carefully the presence of important vessels and organs through the virtual puncture line on the 3D CT image. The identical conventional ultrasound image for virtual ultrasound was depicted and a radiofrequency ablation needle was inserted. Just before inserting the needle, we confirmed the location of the gastric artery on the conventional ultrasound image to ensure that the treatment would be safe (Fig. 1). If the nodule was not visualized clearly because of obstruction by the lung, 500 mL of saline was injected into the right pleural cavity. If the nodule existed close to the major vessels, ethanol was injected using the same technique.

Estimation of Therapeutic Effect

Dynamic CT was performed 3–5 days after treatment. The necrotic area of the HCC nodule and surrounding liver parenchyma

Keywords: caudate lobe, hepatocellular carcinoma, radiofrequency ablation, virtual puncture line

DOI:10.2214/AJR.08.1817

Received September 11, 2008; accepted after revision February 2, 2009.

[1]All authors: Department of Gastroenterology and Metabiology, Ehime University Graduate School of Medicine, Shizukawa 454, Toon-shi, Ehime 791-0295, Japan. Address correspondence to M. Hirooka (masashih@m.ehime-u.ac.jp).

WEB
This is a Web exclusive article.

AJR 2009; 193:W149–W151

0361–803X/09/1932–W149

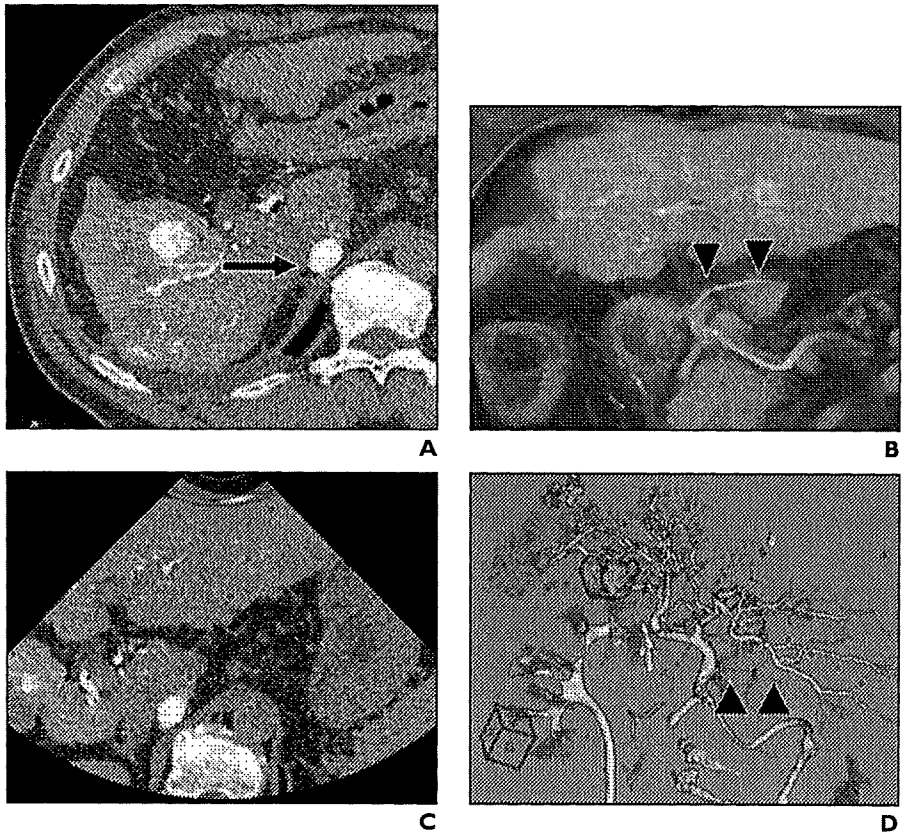

Fig. 1—Creation of virtual puncture line in 56-year-old man with hepatocellular carcinoma arising in Spiegel lobe (case 1).
A, CT during hepatic arteriography shows targeted tumor (*arrow*) in Spiegel lobe.
B, Coronal CT image shows right gastric artery (*arrowheads*) in front of Spiegel lobe.
C, Virtual puncture line is shown by red dotted line on virtual sonogram.
D, Virtual puncture line is also indicated on 3D CT image. This puncture line is away from gastric artery (*arrowheads*), and real puncture through virtual puncture line is safe.

was visualized to be hypoattenuating during the late phases of dynamic CT. The session was defined as the treatment time. All treatments were performed using a virtual puncture line. Repeated dynamic CT was performed every 3 months thereafter, and α-fetoprotein and des-γ-carboxy prothrombin assays were performed before treatment, 1 month after treatment, and every month subsequently.

Results

All 21 patients were treated with radiofrequency ablation (Table 1). However, five nodules were treated with a combination of radiofrequency ablation and ethanol injection because the nodule was close to the extrahepatic major vessels. When the right-side approach was performed, artificial pleural effusion was injected for nine nodules. Of the 12 nodules in the anterior approach, 11 were visualized in the gastric artery on 3D CT. One case that could not be visualized in the gastric artery on 3D images also was not shown on conventional ultrasound. This case was treated carefully, and no complications occurred. There was local recurrence in only one case. Although the treatment of the nodule in the caudate lobe is thought to have a high risk, there were no severe complications in this study. Four cases were treated in overlapping zones with several insertions. These cases also were treated using a virtual puncture line.

Discussion

The central location of the caudate lobe and its intimate relationships with critical vascular structures make it difficult to treat a tumor in this lobe. Local ablation therapy for a tumor in the caudate lobe is highly risky, and the technique for introducing the electrode is difficult. By determining the virtual puncture line before the actual puncture, ablation of the tumor in the caudate lobe can be relatively feasible.

According to the classification of Kumon [1], the caudate lobe consists of three anatomic parts: the Spiegel lobe, the paracaval portion, and the caudate process. The anterior transabdominal approach for nodules in the Spiegel lobe or paracaval portion is often selected. In the anterior approach, the electrode penetrates through the left lobe of the liver, goes into extrahepatic tissue, and then is inserted into the nodule in the caudate lobe. There are a few vessels between the left lobe and the Spiegel lobe, such as the portal vein, hepatic artery, and gastric artery [2, 3]. Of course, it is important to avoid injury to these vessels to avoid severe complications.

The virtual puncture line was useful for confirming whether these important vessels existed on the puncture line. The right-sided approach usually will be selected for the treatment of the nodule in the caudate process. However, the right hepatic vein and major branch of the right portal vein may interfere in this right-sided approach. In this approach, the virtual puncture line was also useful to avoid penetrating these vessels.

Yamakado et al. [4] treated these nodules under CT–fluoroscopic guidance. Radiofrequency ablation under CT–fluoroscopic guidance is often a troublesome treatment. Ideally, radiofrequency ablation is completed under sonographic guidance. Thus, it is important to establish the safety of the puncture route on a sonogram. By using virtual ultrasound and 3D CT images to determine a virtual puncture line that is away from major vessels before radiofrequency ablation, we can perform the radiofrequency ablation

TABLE 1: Hepatocellular Carcinoma Nodules in Study

Case No.	Sex	Age (y)	Child-Pugh Classification	Tumor Diameter (mm)	Location	Approach	No. of Sessions	Local Recurrence
1	M	56	B	15	Spiegel lobe	Anterior	1	No
2	M	76	A	31	Paracaval portion	Anterior	1	No
3	M	79	A	25	Paracaval portion	Right	1	No
4	M	63	A	18	Spiegel lobe	Anterior	1	No
5	M	63	A	15	Paracaval portion	Right	1	No
6	M	82	A	20	Caudate process	Right	2	No
7	M	57	B	18	Paracaval portion	Right	2	No
8	M	57	B	14	Spiegel lobe	Anterior	1	Yes
9	M	60	A	12	Spiegel lobe	Anterior	1	No
10	F	75	A	16	Paracaval portion	Right	1	No
11	F	58	B	23	Spiegel lobe	Anterior	1	No
12	M	80	A	20	Spiegel lobe	Anterior	1	No
13	M	80	A	34	Spiegel lobe	Anterior	2	No
14	M	59	B	23	Caudate process	Right	1	No
15	F	61	A	21	Paracaval portion	Right	1	No
16	M	74	A	40	Spiegel lobe	Right	3	No
17	M	71	A	20	Spiegel lobe	Anterior	2	No
18	M	77	A	17	Paracaval portion	Right	2	No
19	M	55	B	31	Spiegel lobe	Anterior	2	No
20	F	75	B	22	Caudate process	Right	1	No
21	M	63	A	12	Spiegel lobe	Anterior	1	No

safely with conventional ultrasound corresponding to the virtual ultrasound images.

Surgical resection is the most curative treatment for HCC nodules. Technically, the operation is difficult and is more commonly done in conjunction with resection of other portions of the liver [5]. Percutaneous local ablation therapy is less invasive. The residual local recurrence rate is high after subsegmental chemoembolization for HCC in the caudate lobe [6]. In this study the local recurrence rate was very low (2.8%).

In conclusion, treatment of HCC nodules in the caudate lobe using a virtual puncture line is feasible.

References

1. Kumon M. Anatomy of the caudate lobe with special reference to portal vein and bile duct [in Japanese]. *Acta Hepatologica Japonoca* 1985; 26:1193–1199
2. Shibata T, Maetani Y, Ametani F, et al. Efficacy of nonsurgical treatments for hepatocellular carcinoma in the caudate lobe. *Cardiovasc Intervent Radiol* 2002; 25:186–192
3. Ishiko T, Beppu T, Sugiyama T, et al. Radiofrequency ablation with hand-assisted laparoscopic surgery for the treatment of hepatocellular carcinoma in the caudate lobe. *Surg Laparosc Endosc Percutan Tech* 2008; 18:272–276
4. Yamakado K, Nakatsuka A, Akeboshi M, et al. Percutaneous radiofrequency ablation for the treatment of liver neoplasms in the caudate lobe left of the vena cava: electrode placement through the left lobe of the liver under CT–fluoroscopic guidance. *Cardiovasc Intervent Radiol* 2005; 28:638–640
5. Tanaka S, Shimada M, Shirabe K, et al. Surgical outcome of patients with hepatocellular carcinoma originating in the caudate lobe. *Am J Surg* 2005; 190:451–455
6. Terayama N, Miyayama Y, Tatsu H, et al. Subsegmental transcatheter arterial embolization for hepatocellular carcinoma in the caudate lobe. *J Vasc Interv Radiol* 1998; 9:501–508

Hepatology Research 2009; 39: 954–962 doi: 10.1111/j.1872-034X.2009.00537.x

Original Article

Usefulness of the hyperechoic rim for assessing the therapeutic efficacy of radiofrequency ablation in hepatocellular carcinoma patients

Takahide Uehara, Masashi Hirooka, Yoshiyasu Kisaka, Masanori Abe, Yoichi Hiasa and Morikazu Onji

Department of Gastroenterology and Metabology, Ehime University Graduate School of Medicine

Aim: During radiofrequency ablation (RFA) for hepatocellular carcinoma (HCC), a hyperechoic rim develops around the HCC nodules. The usefulness of the hyperechoic rim to guide treatment was assessed.

Methods: RFA was first performed in pig livers to determine the significance of the hyperechoic rim. Fifty-five patients with 75 HCC nodules had received RFA for the treatment of HCC. For those patients, we evaluated whether conventional ultrasonography (US) could be used instead of contrast-enhanced computed tomography (CECT) and contrast-enhanced ultrasonography (CEUS) using virtual imaging. Finally, 31 patients with 45 HCC nodules received RFA, and the degree of ablation was assessed based on the hyperechoic rim. Repeated RFA was done when ablation appeared incomplete.

Results: In the pig livers, the hyperechoic rim was found to be related to the presence of dead cells. The preliminary study showed that US could be used instead of CECT and CEUS to evaluate the degree of ablation caused by RFA. Because hepatic vessels in the back side of the hyperechoic rim were not clear by the artifact, we used the distance from the surface of the liver to the hyperechoic rim for evaluation. By analyzing the extent of the hyperechoic rim, it was noted that incomplete ablation was achieved in 17 of 31 patients (21 of 45 HCC nodules). These patients were re-treated with RFA within 5–15 min of the first RFA.

Conclusion: This study shows that the hyperechoic rim is related to the presence of dead and necrotic tissues. Thus, assessment of the hyperechoic rim's characteristics allows one to evaluate the efficacy of RFA.

Key words: hepatocellular carcinoma, hyperechoic rim, radiofrequency ablation

INTRODUCTION

HEPATOCELLULAR CARCINOMA (HCC) is one of the most common malignant tumors worldwide.[1,2] Whenever possible, the HCC nodules are resected surgically.[3,4] Unfortunately, hepatic resection can be performed in only a small percentage of patients due to patients' lack of hepatic reserve caused by coexisting cirrhosis or the presence of multiple nodules. Thus, percutaneous ethanol injection (PEI),[5,6] microwave coagulation therapy (MCT),[7] and radiofrequency ablation (RFA)[8,9] are used as percutaneous local treatments for unresectable small HCC. Of these approaches, RFA is now widely used to treat HCC nodules, especially small HCC nodules, around the world.[10] Contrast-enhanced computed tomography (CECT) is usually performed 3–4 days after RFA to assess its therapeutic efficacy.[11,12] If residual HCC nodules are detected by CECT, a second round of RFA is performed, usually 4–5 days after the first RFA.

Recently, we reported that abdominal contrast-enhanced ultrasonography (CEUS) may be used instead of CECT to assess the efficacy of RFA in HCC patients.[13] In that study, we found that, on conventional ultrasonography (US), a hyperechoic rim was seen around the necrotic area approximately 5–15 min after RFA. Because this hyperechoic rim resembles the necrotic area depicted by CECT and CEUS, it could likely be used to evaluate whether the RFA had completely destroyed the HCC nodules. This knowledge would help determine the need for further RFA treatment. However, prior

Correspondence: Dr Masashi Hirooka, Department of Gastroenterology and Metabology, Ehime University Graduate School of Medicine, Shitsukawa, Toon, Ehime 791-0295, Japan. Emai: masashih@m.ehime-u.ac.jp

Received 30 November 2008; revision 1 April 2009; accepted 10 April 2009.

to using this finding clinically, the nature of the hyperechoic rim and whether the hyperechoic rim represents the necrotic area need to be determined. Also, the clinical significance of the hyperechoic rim requires confirmation in clinical trials.

Thus, in order to achieve these objectives, we first tried to identify what kind of histological changes are reflected from the image of then hyperechoic rim. Then, based on the findings, we did a clinical study to identify that the hyperechoic rim could be used to evaluate the treated region by RFA for the patients with HCC.

METHODS

Pathological analysis of the hyperechoic rim in pig liver after RFA

APPROVAL WAS OBTAINED from the animal institutional review board for all experiments reported in this study. Two Yorkshire pigs (weighing 67 and 64 kg) were used for the study. The pigs were given general anesthesia; induction was achieved using an i.m. injection of 5 mg/kg ketamine hydrochloride (Nomopain injection; Meiji Seika, Tokyo, Japan) and 4 mg/kg xylazine (Celactal; Bayel Medical, Tokyo, Japan). The animals were then intubated, and atropine sulfate (Atropine sulfate injection; Fuso Pharmaceutical Industries, Osaka, Japan) was administered i.m. The pigs were given halothane (Fluothane; Takeda Chemical Industries, Osaka, Japan) by inhalation and placed in the supine position. The right upper quadrant and epigastrium were shaved and sterilized, and grounding pads were placed on the animal's thighs. A 17-G expandable radiofrequency needle (LeVeen Electrode; Boston Scientific Japan, Tokyo, Japan) was used. Ablation sites in the liver parenchyma were chosen that were away from the liver surface, large vessels and fissures. During RFA, US (LOGIC 400; GE Medical Systems, Tokyo, Japan) images were obtained to monitor hyperechoic change (Fig. 1a). After ablation, the visualized area of coagulation necrosis was examined in the section along the electrode tract that had the maximal degree of necrosis (Fig. 1b). The lengths of the major (perpendicular to the electrode) and minor (along the electrode tract) axes were measured. The US probe was maintained in the same position until the hyperechoic rim was appeared. After the width of the hyperechoic rim and ablated area was measured, the RFA needle was removed. On the line of major axis, the ablated area was defined from the external margin of the one side of the hyperechoic rim to another side of the hyperechoic rim by US (Figs 1a, 2).

Two biopsy specimens were obtained from the pig livers. One specimen was fixed in 10% formalin, sectioned and stained with hematoxylin–eosin. The other specimen was frozen at the optimal cutting temperature using liquid nitrogen to assess tissue viability using nicotinamide-adenine dinucleotide phosphate (NADPH)-diaphorase.[14,15]

Patients

We examined 55 patients (35 men and 20 women; age range, 56–84 years; mean age, 70.4 ± 8.4 years) with 75 HCC nodules, who had been admitted to the Department of Gastroenterology and Metabolism, Ehime University Graduate School of Medicine, Japan, between January 2006 and October 2007. The etiology of their liver cirrhosis was hepatitis B in six patients, hepatitis C in 46 patients and primary biliary cirrhosis in three patients. Based on the Child–Pugh classification of liver dysfunction, 11 patients were class A and nine patients were class B. A preliminary study was done in 24 patients with 30 HCC nodules to determine the correlation between CECT and CEUS for the assessment of the hyperechoic rim.

In the remaining 31 patients with 45 HCC nodules, RFA was done, and the efficacy of RFA was assessed within 5–15 min by US. On the basis of the presence and extent of the hyperechoic rim, re-treatment with RFA was done in 17 of 31 patients (21 of 45 HCC nodules) within 5–15 min of the first RFA.

Imaging methods

Ultrasonography during RFA showed a hyperechoic area that changed to the hyperechoic rim approximately 5–15 min after RFA. CEUS was performed using an APLIO XV (Toshiba, Tokyo, Japan) equipped with a 4-MHz convex array transducer 3–4 days after RFA. The US contrast agent used in this study was SH U 508 A (Levovist; Schering, Berlin, Germany) at a dose of 300 mg/dL. Five minutes after the injection of SH U 508A, the ablated area visualized as a homogenous non-enhanced area was evaluated. CECT (Light Speed Ultra16; GE Medical Systems) was performed 3–4 days after RFA. Multiplanar reconstruction (MPR) using multi-detector row CT (MDCT) was performed using a virtual US (VUS) image. The VUS image was created using Virtual Place Advance (AZE, Tokyo, Japan).[16,17] For scanning, the section thickness was 0.625 mm, and the helical pitch was 1.75.

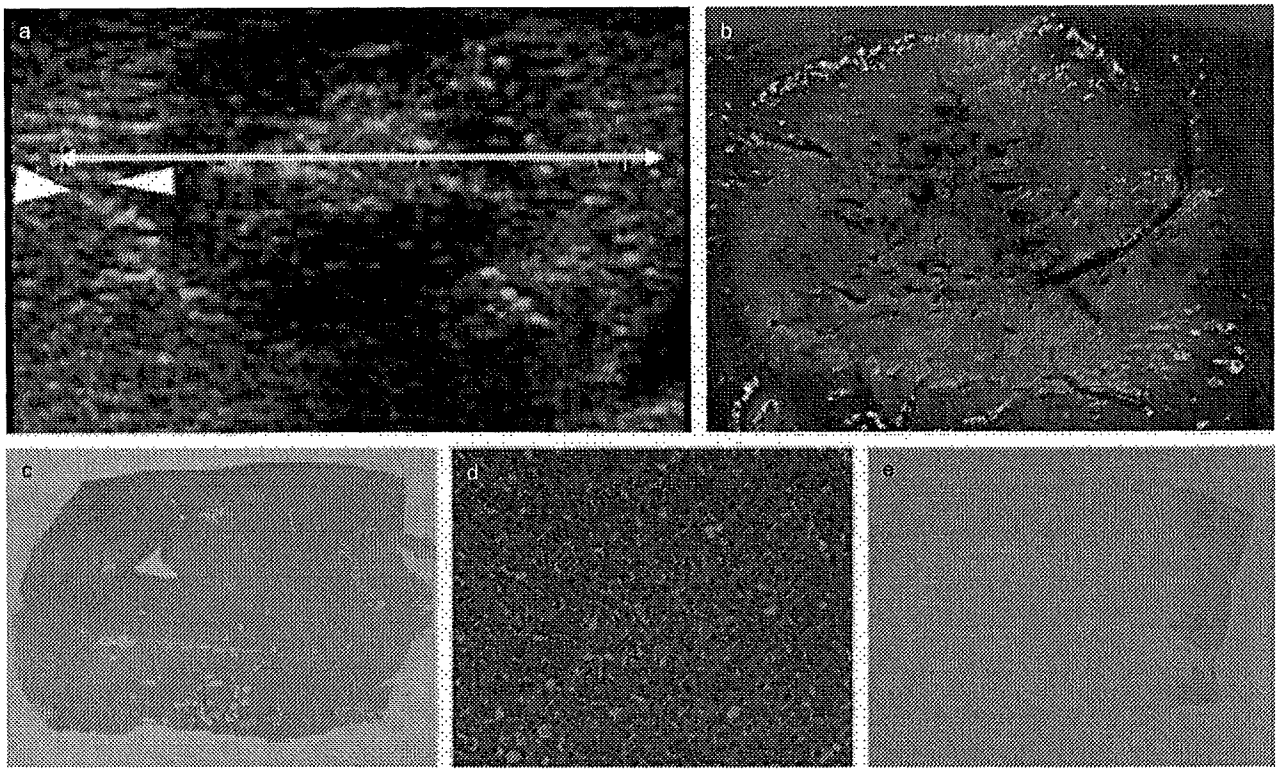

Figure 1 Evaluation of the hyperechoic rim comparison with the histological findings. (a) The hyperechoic rim (white arrow head) is seen in the pig liver after ablation. The maximal width of ablated area was measured (white arrow). (b) After radiofrequency ablation, the section with the maximal damage was cut. (c) The ablated tissue was examined after hematoxylin–eosin staining. (d) Microscopic findings of the red layer seen in (b) are shown. The hemorrhagic area is seen (original magnification ×400). (e) This hemorrhagic area showed no cellular viability on nicotinamide-adenine dinucleotide phosphate-diaphorase staining.

Hyperechoic rim corresponds to imaging findings

In 24 patients with 30 HCC nodules, the hyperechoic rim was evaluated on the VUS and CEUS images. The lengths of the long and short axes were measured at the section showing the maximal hyperechoic area just after the ablation and hyperechoic rim on the US images, and the length of the hyperechoic rim was compared to that obtained on the MPR of VUS and the CEUS image.

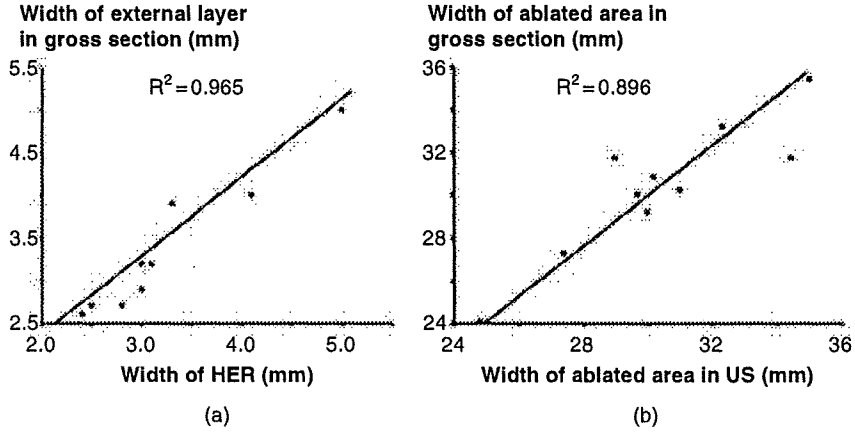

Figure 2 Comparison between the hyperechoic rim (HER) and the gross section. The lengths of the hyperechoic rim (a) and maximal (b) axes of the ablated area on ultrasound (US) corresponded to those of the ablated area on the gross section.

RFA in HCC patients based on preclinical studies

Radiofrequency ablation using a Cool-Tip RF system (Radionics, Burlington, MA, USA) and expandable radiofrequency needle was done. Before treatment, 15 mg pentazocine hydrochloride and 25 mg hydroxyzine hydrochloride were administered i.m. Local anesthesia was induced by 5 mL of 1% lidocaine. After ablation, the therapeutic effect was assessed based on the presence of the hyperechoic rim. VUS images were reconstructed using MDCT data obtained prior to RFA. The US image represented the hyperechoic rim in the identical plane that exhibited the maximal section of the tumor on VUS. The position of the tumor was identified by measuring the distance from the edge of the tumor to architectural landmarks (such as surrounding organs, vessels or the edge of the liver) on the VUS image (Fig. 3). If the measurements of the hyperechoic rim obtained by US were not greater than those obtained by

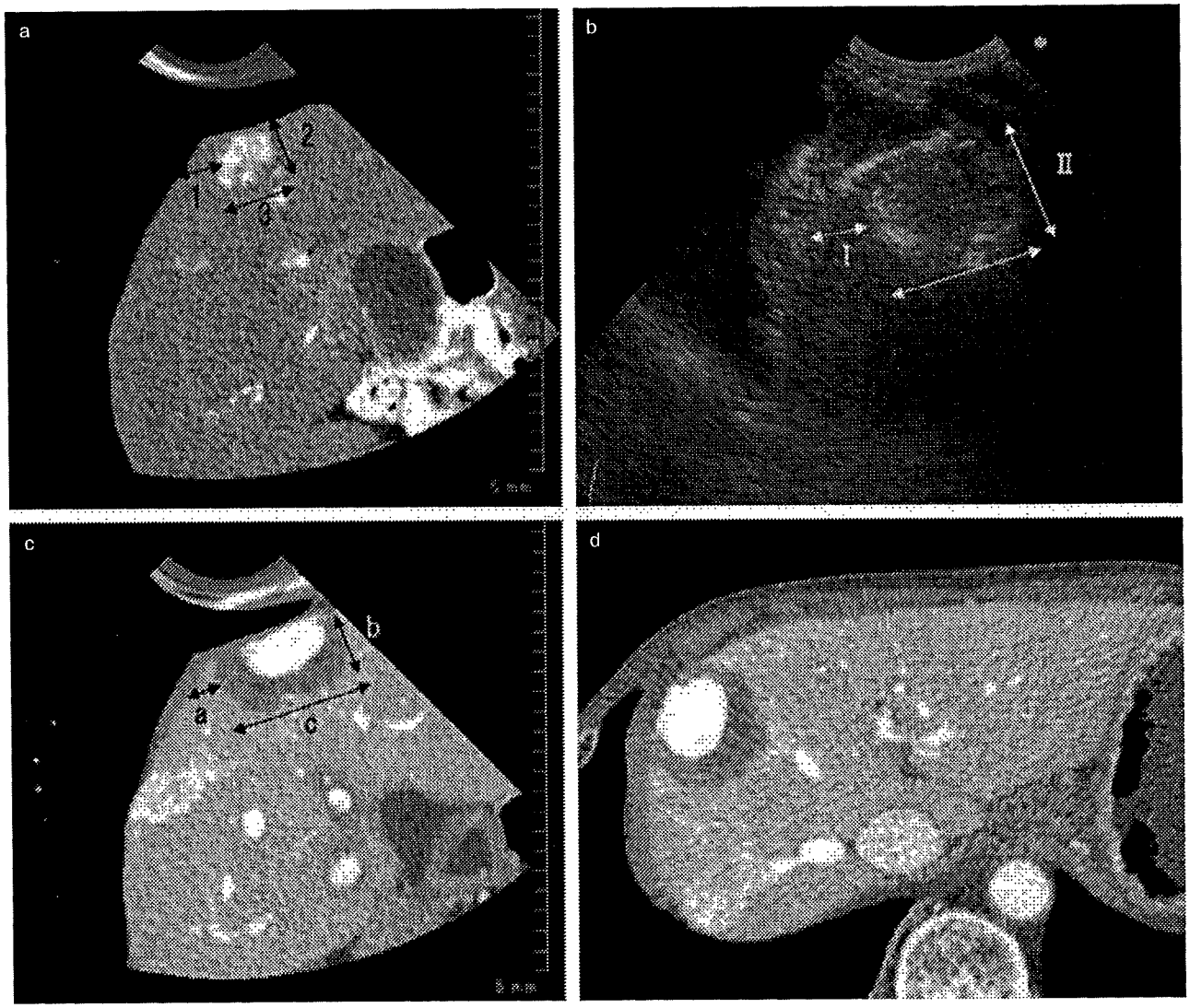

Figure 3 Radiofrequency ablation using the hyperechoic rim. (a) Virtual ultrasonographic (VUS) images were reconstructed using multi-detector row computed tomography (MDCT) data obtained prior to radiofrequency ablation (RFA). (b) The US image represented the hyperechoic rim in the identical plane that exhibited the maximal section of the tumor by VUS. The position of the tumor was identified by measuring the distance from the edge of the tumor to architectural landmarks. (c) VUS image reconstructed by the CT image obtained after RFA resembled (b). (d) In fact, the evaluation of the safety margin by the axial image of CT was enough.

VUS, then the safety margin was considered insufficient and complete necrosis was not achieved. In such cases, additional RFA was performed in the area of the hyperechoic rim. If the nodule was not clearly visualized due to the existence of a hepatic dome, an artificial pleural effusion and/or ascites was induced.[18]

Statistical analysis

Pearson's correlation coefficients were calculated to assess the associations among the length measurements obtained by US (hyperechoic rim), CEUS, VUS image and enucleated tissue. *P*-values of less than 0.05 were considered significant. Cumulative incidence of local tumor progression was calculated using the Kaplan–Meier technique. Data analysis was performed using SPSS ver. 15.0.

RESULTS

Evaluation of the hyperechoic rim caused by RFA in pig liver

GROSS EXAMINATION REVEALED three layers. The central core, which corresponded to the central hyperechoic area, was the darkest area (Fig. 1b); it was thought to be the region in which the RF electrode expanded. The middle layer was white-yellow in color and was related to the middle hypoechoic area. The external layer was red in color and corresponded to the external hyperechoic rim (Fig. 1a,b). The external red layer corresponded to the hyperechoic rim, and was found to be a hemorrhagic area on hematoxylin–eosin staining (Fig. 1c,d). On NADPH-diaphorase staining, no viable cells were detected in the hyperechoic rim (Fig. 1e). Indeed, there were also significant strong correlations in the width of the red layer ($r^2 = 0.965$) and the width of the external margin of the hyperechoic rim ($r^2 = 0.896$) (Fig. 2). Thus, we defined that a hyperechoic rim was reflected with the red layer due to hemorrhagic change by RFA.

RFA in HCC patients

A representative imaging picture of one of the 24 patients with 30 HCC nodules assessed in the preliminary study is shown in Figure 4. US during RFA revealed a hyperechoic area (Fig. 4a). The mean length of the long and short axes of this area were 29.7 ± 3.4 and 25.6 ± 3.0 mm, respectively. This area changed to the hyperechoic rim 5–15 min after RFA (Fig. 4b). The mean length of the long and short axes of this area were 27.4 ± 3.3 and 23.6 ± 2.9 mm, respectively. The hyperechoic rim was compared to the images obtained on CEUS (Fig. 5b) and VUS (Fig. 5c). The lengths of the long and short axes were measured at the maximal section on the hyperechoic rim on CEUS and VUS (Fig. 5). Using a linear model, the correlations between the major and minor lengths of the US hyperechoic rims and the VUS and CEUS images were determined (Fig. 6). The major and minor lengths of the parenchymal defect on CEUS 3 days after RFA had a strong correlation with those of the US hyperechoic rim (major axis, $r^2 = 0.98$; minor axis, $r^2 = 0.91$) (Fig. 5a,b). Similarly, there were significantly strong correlations for the lengths of the major axis ($r^2 = 0.98$) and the minor axis ($r^2 = 0.87$) at the maximal section between the US hyperechoic rim and VUS images (Fig. 6c,d).

The imaging profile of a representative case of the nine patients with 15 HCC nodules in which the clinical utility of the hyperechoic rim was assessed is shown in

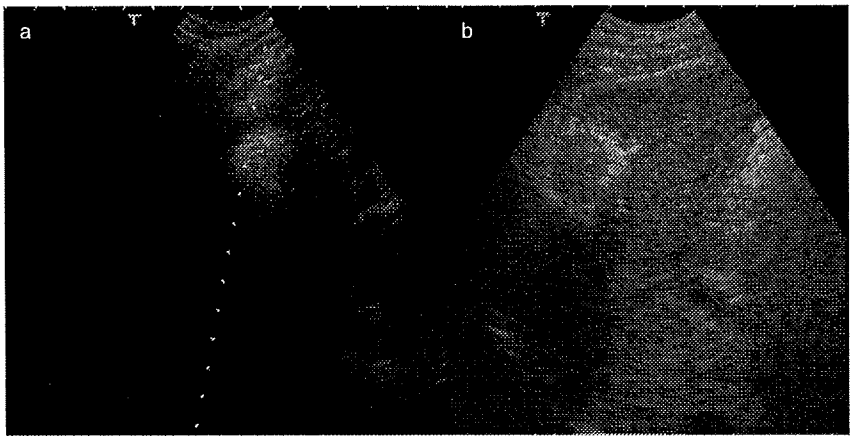

Figure 4 Hyperechoic change on conventional ultrasonography. (a) A hyperechoic area appeared immediately after radiofrequency ablation. (b) Five minutes after radiofrequency ablation, the hyperechoic rim is seen on ultrasonography.

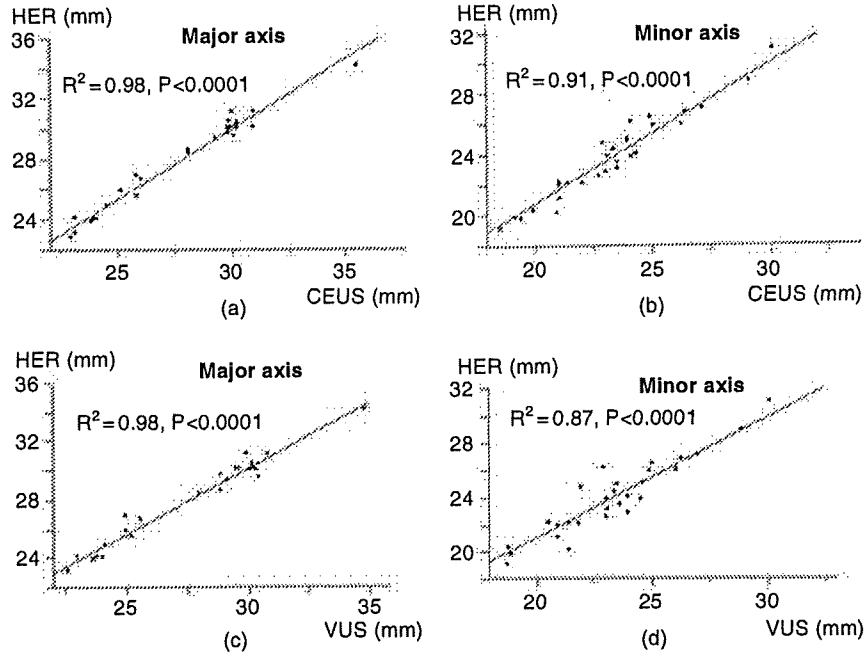

Figure 5 Contrast-enhanced ultrasonography and virtual ultrasonography images. (a) Five minutes after radiofrequency ablation, the hyperechoic rim (HER) is seen by ultrasonography. (b) The perfusion defect on contrast-enhanced ultrasonography performed during the presence of the hyperechoic rim corresponds to the external margin of the rim. (c) The perfusion defect on virtual ultrasonography performed 3 days after radiofrequency ablation is seen.

HER: hyper echoic rim, CEUS: contrast enhanced ultrasonography
VUS: virtual ultrasonography

Figure 6. The position of the tumor was identified by measuring the distance from the edge of the tumor to the architectural landmark on the VUS image (Fig. 7b). The same distance was measured on US from the edge of the hyperechoic rim to the architectural landmark (Fig. 7c). If the distance measured on the US was not longer than the distance measured on the VUS image, the safety margin was considered insufficient and complete necrosis was not achieved (Fig. 7d). The cumulative local recurrence rate is shown in Table 1.

Only two cases of local lesion recurrence were found, and both cases had HCC, the diameters of which were more than 25 mm.

Table 1 Cumulative local recurrence rate after radiofrequency ablation

	All nodules	Tumor diameter (mm)		
		≤ 19	20–24	25≥
n	45	33	5	7
Time after radiofrequency ablation				
6 months	0%	0%	0%	0%
12 months	2.2%	0%	0%	14.5%

DISCUSSION

ALTHOUGH RFA IS an effective method for treating these patients, it has some limitations. It is difficult to destroy entire HCC nodules by one session of RFA treatment, and an additional session of RFA is usually needed. However, the assessment of the initial RFA is usually checked 3–4 days later, and then additional RFA, if required, is subsequently performed. This increases hospital lengths of stay and compromises patients' quality of life. If the efficacy of RFA could be assessed during the initial RFA, supplementary RFA could be done during the same session. In this study, RFA was first done in the pig liver to identify a marker for the degree of ablation achieved by RFA. Our study revealed that a hyperechoic rim was detected within 5–15 min after RFA, which represented the extent of ablation achieved by RFA. A complete hyperechoic rim indicated that the HCC tissues were satisfactorily destroyed. The new contribution of this study is the finding that the hyperechoic rim could be assessed using conventional US. The usefulness of conventional US was confirmed by comparing its results to those of VUS and CEUS. Nouso *et al.* reported that hyperechoic change was correlated with a CEUS perfusion defect.[19] In

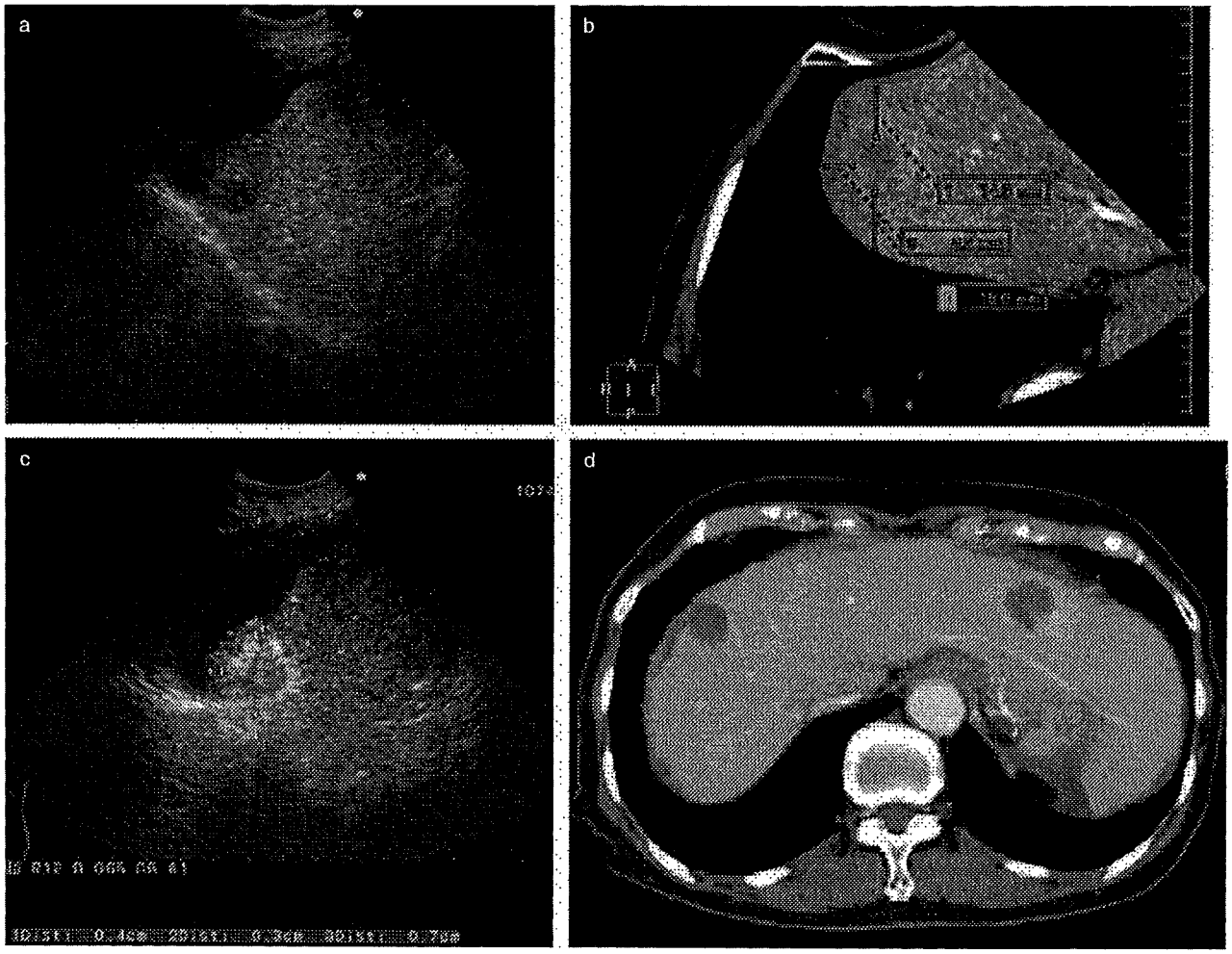

Figure 6 Comparisons among the ultrasonography hyperechoic rim, contrast-enhanced ultrasonography, and virtual ultrasonography. (a) The length of the major axis of the hyperechoic rim has a strong correlation with the perfusion defect of contrast-enhanced ultrasonography. (b) That of the minor axis of the hyperechoic rim had a strong correlation. That of the major (c) and minor (d) axes of the hyperechoic rim corresponded to those of virtual ultrasonography as well.

fact, hyperechoic change was seen on US immediately after RFA, but this hyperechoic area gradually changed into the smaller hyperechoic rim a few minutes after RFA. The hyperechoic rim can be visualized for 5–15 min. Thus, the characteristics of the hyperechoic rim were analyzed and subsequently used to direct treatment. It is difficult to correlate US images to those of axial CT images. Imai *et al.* reported that the CEUS perfusion defect corresponded with the CT perfusion defect.[20] In the present study, the US hyperechoic rim was compared to the CEUS and VUS imaging findings. On CEUS performed during the presence of the hyperechoic rim, the perfusion defect corresponded to the external margin of the rim. The hyperechoic rim had a strong correlation with the findings on CEUS and VUS imaging (Fig. 6). In the present animal study, the hyperechoic rim represented the hemorrhagic area seen on the section stained with hematoxylin–eosin. Furthermore, viable cells were not detected in the hyperechoic region on NADPH-diaphorase staining (Fig. 4e). Thus, the hyperechoic rim was considered to be the necrotic area. The present study found that, by examining the characteristics of the hyperechoic rim, additional ablation could be performed immediately after the initial ablation if needed; this can significantly shorten the hospital stay. Indeed, RFA was completed in 29 of 31 patients (42 of 45 HCC nodules) within 1 day. It is difficult to assess tumors that are located far from the liver surface,

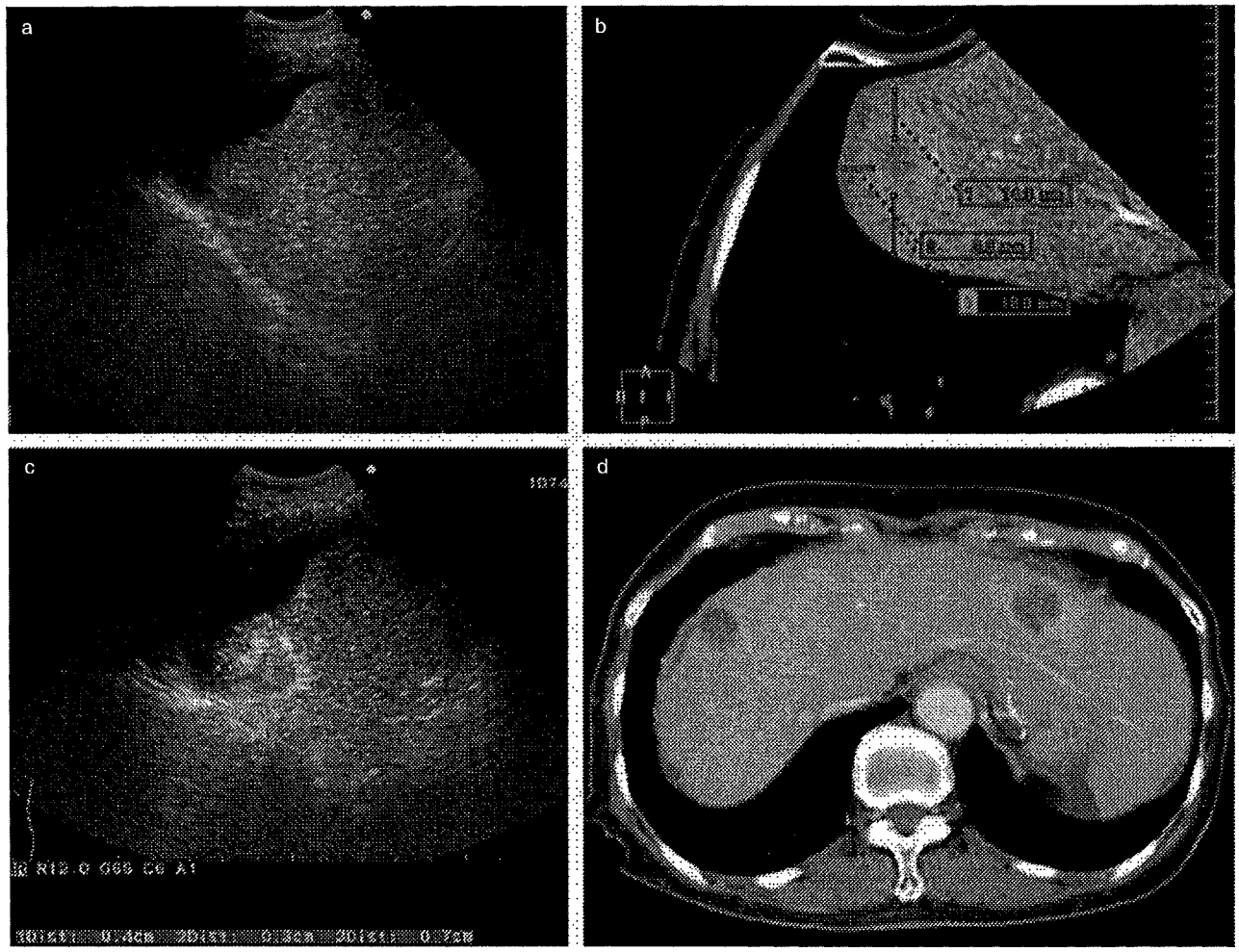

Figure 7 Clinical experience using the hyperechoic rim. (a)The tumor is located in the hepatic dome. (b) The computed tomography virtual ultrasound image prior to radiofrequency ablation. (c) By referencing (b), the hyperechoic rim can be seen to surround the tumor. (d) Computed tomography images obtained after radiofrequency ablation show that an adequate safety margin was achieved.

because the perfusion defect is not clearly seen on CEUS. However, even in such cases, the hyperechoic rim is depicted on US. If the tumor is located far from the liver surface, the imaging findings are clearer on US than on CEUS. Only three patients were given two RFA treatments. In one of these patients, the tumor was located in the hepatic dome and no obvious architectural landmarks were visualized around the tumor. In fact, the VUS image was not reconstructed accurately in this patient. The hyperechoic rim does not always reflect the ablation area accurately. Hepatic vessels in the back side of the hyperechoic rim were not clear by the artifact. So, sometimes it is difficult to evaluate whether we could get enough of a safety margin by the measurements from these vessels. However, it is easy to identify the shape of the liver in the back side of the hyperechoic rim (Figs 2–5). We used the distance from the surface of the liver to the hyperechoic rim for evaluation. Because by only a slight shake of the US slice it is possible that VUS images do not completely correspond to US images, we believe that a landmark of ablation area was needed and the hyperechoic rim was useful for this landmark.

Though the hyperechoic rim was represented by the red external layer of the ablated area in our study, this hyperechoic rim was thought to be the air induced by ablation. Especially hyperechoic change just after ablation was significantly larger than the hyperechoic rim. Thus, we thought that hyperechoic change reflected the

gas. Because the hyperechoic rim was more similar to ablated area, it is efficacious to use this hyperechoic rim. Only two cases had local lesion recurrence (Table 1). In those cases, the diameter of the nodule was more than 25 mm. In this study, we considered that a safety margin of at least 5 mm should be achieved. The wider safety margin (> 5 mm) might be required for the treatment of larger HCC nodules, especially with a diameter of more than 25 mm.

In conclusion, the hyperechoic rim on US represents the necrotic area. Hepatic vessels in the back side of the hyperechoic rim were not clear by the artifact, however, we could evaluate the safety margin by using the distance from the surface of the liver to the hyperechoic rim. Assessment of the hyperechoic rim's characteristics allows one to evaluate the efficacy of RFA. Moreover, it is possible to perform repeat RFA within a short time by evaluating the presence and extent of the hyperechoic rim on US.

REFERENCES

1 El-serag HB, Mason AC. Rising incidence of hepatocellular carcinoma in the United states. *N Engl J Med* 1999; 340: 745–50.
2 Taylor-Robinson SD, Foster GR, Arora S, Hargreaves S, Thomas HC. Increase in primary liver cancer in the UK, 1979–94. *Lancet* 1997; 350: 1142–3.
3 Yamasaki S, Hasegawa H, Makuuchi M, Takayama T, Kosuge T, Shimada K. Choice of treatments for small hepatocellular carcinoma: hepatectomy, embolization or ethanol injection. *J Gastroenterol Hepatol* 1991; 6: 408–13.
4 Kanematsu T, Matsumata T, Shirabe K *et al.* A comparative study of hepatic resection and transcatheter arterial embolization for the treatment of primary hepatocellular carcinoma. *Cancer* 1993; 71: 2181–6.
5 Akamatsu K, Miyauchi S, Ohkubo K, Maruyama M. Development and evaluation of a needle for percutaneous ethanol injection therapy. *Radiology* 1993; 186: 284–6.
6 Shiina S, Yasuda H, Muto H *et al.* Percutaneous ethanol injection in the treatment of liver neoplasms. *AJR* 1987; 149: 949–52.
7 Seki T, Wakabayashi M, Nakagawa T *et al.* Ultrasonically guided percutaneous microwave coagulation therapy for small hepatocellular carcinoma. *Cancer* 1994; 74: 817–25.
8 Rossi S, Di Stasi M, Buscarini E *et al.* Percutaneous RF interstitial thermal ablation in the treatment of hepatic cancer. *AJR* 1996; 167: 759–68.
9 Giorgio A, Tarantino L, de Stefano G *et al.* Percutaneous sonographically guided saline-enhanced radiofrequency ablation of hepatocellular carcinoma. *AJR* 2003; 181: 479–84.
10 Horiike N, Iuchi H, Ninomiya T *et al.* Influencing factors for recurrence of hepatocellular carcinoma treated with radiofrequency ablation. *Oncol Rep* 2002; 9: 1059–62.
11 Solbiati L, Ierace T, Goldberg SN *et al.* Percutaneous US – guided radio – frequency ablation of liver metastases: treatment and follow – up in 16 patients. *Radiology* 1997; 202: 195–203.
12 Livraghi T, Goldberg SN, Monti F *et al.* Saline – enhanced radio – frequency tissue ablation in the treatment of liver metastases. *Radiology* 1997; 202: 205–10.
13 Kisaka Y, Hirooka M, Kumagi T *et al.* Usefulness of contrast-enhanced ultrasonography with abdominal virtual ultrasonography in assessing therapeutic response in hepatocellular carcinoma treated with radio frequency ablation. *Liver Int* 2006; 26: 1241–7.
14 Morimoto M, Sugimori K, Shirato K *et al.* Treatment of hepatocellular carcinoma with radiofrequency ablation: radiologic – histologic correlation during follow – up periods. *Hepatology* 2002; 35: 1467–75.
15 Neumann RA, Knobler RM, Pieczkowski F, Gebhart W. Enzyme histochemical analysis of cell viability after argon laser – induced coagulation necrosis of the skin. *J Am Acad Dermatol* 1991; 25: 991–8.
16 Hirooka M, Iuchi H, Kurose K *et al.* Abdominal virtual ultrasonographic images reconstructed by multi-detector row helical computed tomography. *Eur J Radiol* 2005; 53: 312–17.
17 Hirooka M, Iuchi H, Kumagi T *et al.* Virtual sonographic radiofrequency ablation of hepatocellular carcinoma visualized on CT but not on conventional sonography. *AJR* 2006; 186: 255.
18 Uehara T, Hirooka M, Ishida K *et al.* Percutaneous ultrasound – guided radiofrequency ablation of hepatocellular carcinoma with artificially induced pleural effusion and ascites. *J Gastroenterol* 2007; 42: 306–11.
19 Nouso K, Shuraga K, Uematsu S *et al.* Prediction of the ablated area by the spread of microbubbles during radiofrequency ablation of hepatocellular carcinoma. *Liver Int* 2005; 25: 967–72.
20 Imai Y, Okamoto N, Tateiwa N *et al.* Assessment of treatment efficacy in radiofrequency ablation for hepatocellular carcinoma: comparison between multiplanar reconstruction by multi – detector row CT and contrast – enhanced ultrasonography by Truagent detection mode. *Hepatol Res* 2006; 35: 69–75.

Digestive Endoscopy (2009) **21**, 82–86 doi:10.1111/j.1443-1661.2009.00836.x

ORIGINAL ARTICLE

EFFICACY OF LAPAROSCOPIC RADIOFREQUENCY ABLATION FOR HEPATOCELLULAR CARCINOMA COMPARED TO PERCUTANEOUS RADIOFREQUENCY ABLATION WITH ARTIFICIAL ASCITES

MASASHI HIROOKA,[1] YOSHIYASU KISAKA,[1] TAKAHIDE UEHARA,[1] KIYOTAKA ISHIDA,[1] TERU KUMAGI,[1] YUJI WATANABE,[2] MASANORI ABE,[1] BUNZO MATSUURA,[1] YOICHI HIASA[1] AND MORIKAZU ONJI[1]

[1]*Department of Gastroenterology and Metabology and* [2]*Department of Organ Regenerative Surgery, Ehime University Graduate School of Medicine, Ehime, Japan*

Aim: Hepatocellular carcinoma (HCC) nodules close to the liver surface exhibit high recurrence compared to those in distal parts of the liver. Moreover, when nodules remain adjacent to the gastrointestinal tract or gallbladder, severe complications such as perforation of those organs may occur due to invasive therapy. Percutaneous radiofrequency ablation (PRFA) with artificial ascites or laparoscopic radiofrequency ablation (LRFA) are used to treat these patients to avoid complications. The purpose of the present study was to assess the efficacy and safety of these two methods.
Methods: Subjects comprised 74 patients (48 men, 26 women; mean age, 68.5 ± 8.0 years; range, 46–89 years) with 86 HCC nodules. PRFA with artificial ascites was carried out for 37 patients (44 nodules) and LRFA was used for 37 patients (42 nodules). Clinical profiles were compared between groups.
Results: No significant differences in clinical profiles were found between patients treated by PRFA or LRFA. Mean number of treatments was significantly lower for LRFA (1.0 ± 0.0) than for PRFA (2.1 ± 1.0, $P < 0.001$). Mean number of PRFA treatments was 2.2 ± 1.0 in patients with HCC nodules >2 cm in diameter, whereas all tumors were completely ablated with only one session of LRFA. The safety margin was significantly wider for LRFA than for PRFA.
Conclusion: LRFA is a better treatment option for ablation of HCC nodules >2.0 cm in diameter.

Key words: artificial ascites, hepatocellular carcinoma, laparoscopic radiofrequency ablation, percutaneous radiofrequency ablation.

INTRODUCTION

Hepatocellular carcinoma (HCC) is one of the most common neoplasms in Japan. Surgical resection is considered as one of the most effective therapeutic regimens for preventing local recurrence, but is limited by liver dysfunction and tumor multiplicity. Non-surgical treatments such as percutaneous ethanol injection (PEI),[1,2] percutaneous microwave coagulation therapy (PMCT)[3] and radiofrequency ablation (RFA)[4,5] are thus widely carried out to treat HCC. Of these therapies, RFA is now accepted as the most effective therapeutic approach. However, local recurrence remains problematic in patients with RFA. In particular, nodules close to the liver surface show higher recurrence than other nodules.[6] Moreover, when nodules exist adjacent to the gastrointestinal tract or gallbladder, severe complications such as perforation of those organs may occur.[7–9] Recently, the artificial ascites method has been reported as effective for the treatment of nodules adjacent to the gastrointestinal tract or gallbladder.[10–13] In particular, we have reported that percutaneous RFA (PRFA) with artificial ascites is effective and safe for smaller HCC nodules (diameter <2 cm).[13] Although artificial ascites methods can easily be carried out in small HCC, the number of treatments is increased in cases of larger HCC. Furthermore, ablation cannot be properly carried out due to previous treatment with transcatheter arterial embolization (TAE) or other maneuvers. In such circumstances, laparoscopic RFA (LRFA) may offer a better therapeutic choice.[14,15]

However, little information is available regarding differences between PRFA and LRFA. The present study retrospectively assessed the safety and efficacy of these two therapeutic approaches in patients with HCC.

METHODS

Patients

Subjects comprised 74 patients (48 men, 26 women; mean age, 68.5 ± 8.0 years; range, 46–89 years) with 86 nodules who had been admitted to the Department of Gastroenterology and Metabology, Ehime University Graduate School of Medicine, Japan, between January 2002 and September 2006. Positive results were obtained for hepatitis B surface antigen in 12 patients and hepatitis C virus antibody in 50 patients, but no specific cause could be found in 12 patients (cryptogenic). Child–Pugh classification was class A in 54 patients and class B in 20 patients. Patients with Child–Pugh class C liver cirrhosis, bleeding tendencies, chronic heart disease or chronic pulmonary disease were excluded from this study. Nodules in segment 7 that could not be confirmed directly by

Correspondence: Masashi Hirooka, Department of Gastroenterology and Metabology, Ehime University Graduate School of Medicine, Toon, Ehime 791-0295, Japan. Email: masashih@m.ehime-u.ac.jp

Received 12 August 2008; accepted 10 November 2008.

laparoscopy were also excluded. All nodules in this study were close to the gastrointestinal tract and/or gallbladder. Distance between the tumor surface and liver surface was <5 mm. Mean maximum diameter of the HCC was 25.4 ± 5.7 mm (range, 20–41 mm). The diameter of all nodules was more than 2 cm. Of the 86 nodules, 44 were in the anterior segment, 20 in the posterior segment, 16 in the lateral segment, four in the medial segment, and two in the caudate lobe. HCC was diagnosed from patient history, clinical presentation, biochemical data and results of imaging. Helical dynamic computed tomography (CT), CT hepatic arteriography (CTHA), and CT during arterial portography (CTAP) were used in all patients. All tumors showed the typical pattern of HCC (hyperattenuation in the arterial phase of dynamic CT and CTHA, and hypoattenuation in the portal-venous phase and CTAP). Informed consent was obtained from all subjects prior to treatment.

Transcatheter arterial embolization

The Seldinger technique with local anesthesia was used to access the femoral artery. The catheter was inserted as close as possible to the tumor stain. Iodized oil (Lipiodol; Nihon Schering, Tokyo, Japan) was injected, followed by administration of 1–2 mm cubes of gelatin sponge (Gelfoam; Upjohn, Kalamazoo, MI, USA). TAE was carried out approximately 1 week before RFA.

Radiofrequency ablation

Prior to the start of therapy, we recommended LRFA for all patients with HCC nodules adjacent to the gastrointestinal tract or gallbladder. If the patient agreed, LRFA was carried out. If the patient did not agree to laparoscopy, PRFA was performed. Inducing artificial ascites was impossible in two cases due to adhesions, so those patients were treated using PEI.

Percutaneous radiofrequency ablation with artificial ascites

Before treatment, 15 mg pentazocine hydrochloride and 25 mg hydroxyzine hydrochloride were given i.m. Subjects were given local anesthesia and then a 21-gauge needle was inserted just in front of the surface of the liver to inject 5% glucose. If the distance between the tumor and adjacent organs was less than 5 mm as shown by CT, RFA with artificial ascites was carried out. After achieving approximately 5 mm of fluid space in front of the liver surface, the needle was changed to a 14-gauge needle (Co Access needle; Boston Science, Tokyo, Japan) and 5% glucose was injected rapidly.[13] After producing artificial ascites, we inserted a 20-cm-long 17-gauge radiofrequency electrode equipped with a 2- or 3-cm exposed metallic tip (Cool tip; Radionics, Burlington, MA, USA). Space between the tumor and adjacent structures was confirmed, and ablation was then started (Fig. 1). When adequate space was not achieved, patients were treated using PEI (Fig. 2).

Laparoscopic procedure

Laparoscopic procedures were carried out under general anesthesia. The first trocar for the laparoscope was inserted in the abdominal cavity after insertion of air. Two other trocars were inserted under laparoscopic guidance. If the tumor existed adjacent to the gastrointestinal tract, EndoRetract (Coviden, Mansfield, MA, USA) was inserted to separate the tumor from the gastrointestinal tract. When tumor nodules were adjacent to the gallbladder, RFA was carried out after cholecystectomy. A 7.5 MHz linear-array laparoscopic ultrasound probe (UST-5536-7.5; ALOKA, Tokyo, Japan) was inserted to identify the target tumor and surrounding structures (i.e. hepatic vein, portal vein, bile duct, hepatic artery). If the tumor was not identified directly by adhesion, RFA was carried out after detachment of adhesions (Fig. 3).

Estimation of therapeutic effect

Dynamic CT was carried out between 3 and 5 days after treatment. The necrotic area of the HCC nodule and surrounding liver parenchyma appeared as a hypoattenuating area during late-phase dynamic CT. If the necrotic area depicted on post-treatment dynamic CT was larger than the viable area depicted on pretreatment dynamic CT, therapy was considered successful.[16] Dynamic CT or ultrasonography was repeated every 3 months thereafter until recurrence was detected on imaging. Alpha-fetoprotein and des-γ-carboxy-prothrombin levels were assessed before treatment, 1 month after treatment, and every month thereafter until recurrence was detected.

Statistical analysis

Data are expressed as mean ± standard deviation. Differences in means were analyzed using Student's *t*-test and frequency distribution was compared by χ^2 test. Cumulative recurrence rate was calculated using Kaplan–Meier methods, and differences were compared using log–rank testing. These analyses were carried out using SPSS version 14.0 (SPSS, Chicago, IL, USA).

RESULTS

Adhesion was near the target tumor for six patients (16.2%) in the LRFA group. All nodules were treated by TAE, and all tumors displayed a diameter >2 cm. In the PRFA group, four patients (10.8%) showed adhesion.

No significant differences in clinical profiles were found between PRFA and LRFA groups (Table 1). Mean number of treatments was significantly lower for LRFA (1.0 ± 0.0) than for PRFA (2.1 ± 1.0; $P < 0.001$). Safety margin was significantly wider for LRFA than for PRFA (Table 2). Moreover, the rate of achieving a wide safety margin (>1 cm) was significantly lower with PRFA (4.5%, 2/44) than with LRFA (76.2%, 32/42; $P < 0.05$). Mean duration of hospitalization was significantly shorter for LRFA (15.9 ± 8.4 days) than for PRFA (22.0 ± 11.6 days; $P < 0.05$). Local recurrence rate at 1 and 2 years tended to be higher with PRFA (0% and 17.5%, respectively) than with LRFA (0% each; $P = 0.01$ each). No severe complications were seen in either group within a mean follow-up period.

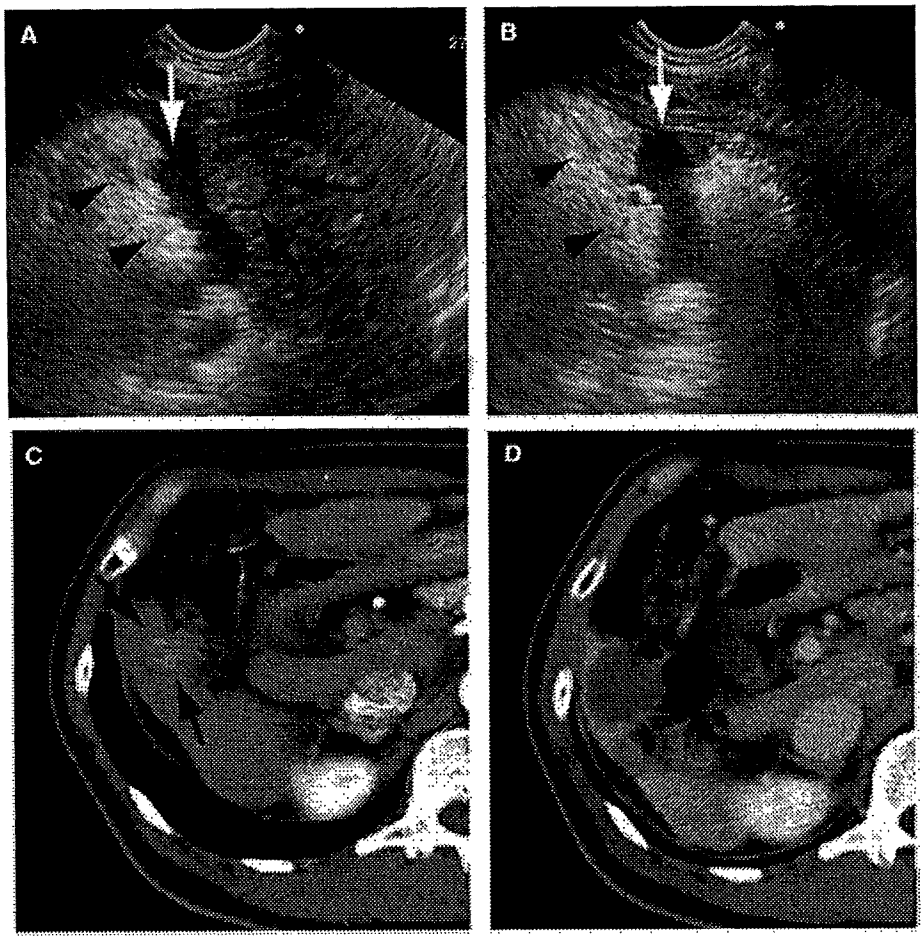

Fig. 1. Percutaneous radiofrequency ablation with artificial ascites. (a) After injection of 5% glucose (white arrow), tumor (black arrows) was separated from the colon (black arrowheads). (b) After ablation, a hyperechoic area (black arrow) appeared. (c) Computed tomography revealed a tumor (black arrows) close to the colon. (d) Tumor was completely ablated.

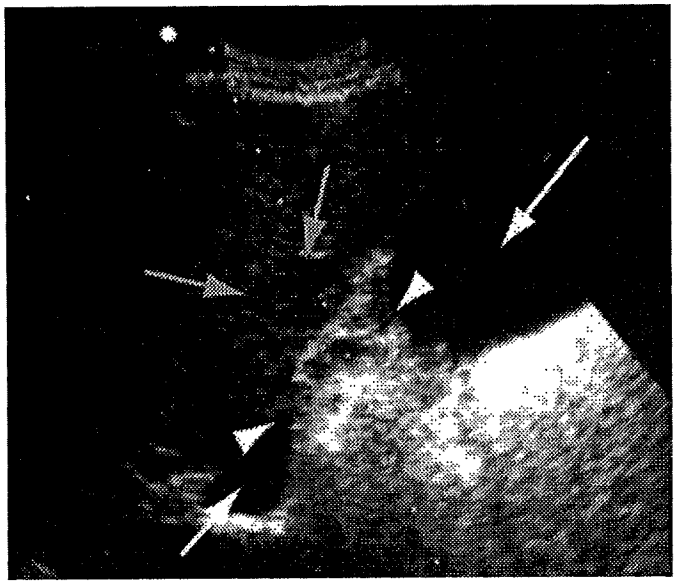

Fig. 2. Adhesion (white arrowhead) is clearly seen between the tumor (gray arrows) and the intestinal tract after injecting artificial ascites (white arrows).

DISCUSSION

Radiofrequency ablation has recently been widely used in HCC patients due to the safety and efficacy of the procedure.[4,5] Some problems have been identified in using RFA for larger HCC close to the liver surface. To ablate these nodules, LRFA,[14,15] thoracoscopy[17] and open surgery[18] have been used. Another approach, PRFA, has also recently been carried out for ablation of such nodules. However, artificial ascites gives rise to some problems. Indeed, no previous reports have compared the merits and demerits of PRFA and LRFA. The present study therefore compared the effects of LRFA and PRFA with artificial ascites.

Although most tumors located away from the liver surface can be ablated safely and easily by PRFA, similar outcomes are difficult to achieve when the tumor is located near the surface. Moreover, RFA is difficult when tumors exist near organs such as the gallbladder and gastrointestinal tract and may induce severe complications.[7–9] PRFA with artificial ascites has recently been reported as a non-invasive method.[10–13] When a method with artificial ascites is performed, damage to the abdominal wall and adjacent organs can be avoided by separating the ablation area and adjacent structures. However, we encountered patients for whom injection of artificial ascites cannot be carried out due to adhesions. Such adhesions were attributed to previous treatment with RFA or PEI. When RFA is carried out for larger nodules, TAE is performed prior to RFA to prevent a cooling effect.[19,20] Adhesions are thus often formed in larger nodules. Although we reported the efficacy of PRFA with artificial ascites, the study population was small (mean tumor diameter, 16.9 ± 7.0 mm).